EVIDENCE OF RING-FAULTS IN ORIENTALE FROM GRAVITY

by

Yaser Kattoum

A thesis submitted to the Faculty and the Board of Trustees of the Colorado School of Mines in partial fulfillment of the requirements for the degree of Master of Science (Geophysics).

Golden, Colorado

Date _____

Signed: _____
Yaser Kattoum

Signed: _____
Jeff Andrews-Hanna
Thesis Advisor

Golden, Colorado

Date _____

Signed: _____
Dr. Terence K. Young
Professor and Head
Department of Geophysics

ABSTRACT

The Orientale basin on the Moon is a well-preserved multi-ring impact basin that spans 900 km in diameter at its outermost ring. It consists of three concentric ring structures known as the Inner Rook, Outer Rook, and Cordillera . Orientale has been the focus of attempts to understand ring formation mechanisms because of its well-defined structure. Based on inwardly dipping faces consistent with the morphology of fault scarps, the Cordillera ring has been interpreted as forming through listric normal faulting from the inward collapse of the interior basin. A similar mechanism may have been responsible for the formation of the Outer Rook, though it has also been interpreted as the rim corresponding to the collapsed excavation cavity. This study uses gravity and topography data to examine the internal crustal structure of Orientale using a Monte Carlo Markov Chain approach to find the best-fit fault dip and displacement, as well as the depth to an intracrustal density interface and the density contrast across that interface. The best-fit solution for the case of both a Cordillera fault and Outer Rook fault has an intracrustal interface depth of 10.8 km, a vertical component of fault displacement fault displacement of 7.8 km, a fault dip of 28 °, and a density contrast of 350 kg/m^3 between the upper and lower crust giving a lower crustal density of 3050 kg/m^3. However, models with faults only at the Cordillera or with faults that do not cross the Moho also provide adequate fits to the data. This analysis presents quantitative evidence for the existence of faults beneath the rings of Orientale. Such analyses can be extended to future higher resolution gravity data sets such as GRAIL to more tightly constrain the subsurface structure of Orientale and other similar basins.

TABLE OF CONTENTS

LIST OF FIGURES

ACKNOWLEDGMENTS

This work was made possible by the NASA LASER grant that was awarded to Jeff Andrews-Hanna. I would like to thank my committee who was comprised of Dr. Jeff Andrews-Hanna, Dr. Tom Davis, Dr. Yaoguo Li, and Dr. Richard Krahenbuhl for their time and comments. Furthermore, I want to thank my lab group whom consist of Dave Horvath, Ezgi Karsozen, Brian Davis, and Johanna Cornelia for giving me constructive criticism on my work and presentations throughout the time I was here. I am also grateful for the time Bill Woodruff and Dr. Myoung Jae Kwon took to discuss Markov Chain Monte Carlo techniques to aid me in my research. Lastly, I want to thank the department head, Dr. Terry Young, and the geophysics department for facilitating a great learning atmoshpere to be in. Parts of this spherical harmonic analysis were performed using the freely available software archive SHTOOLS (shtools.ipgp.fr).

To my parents: Zahra and Naim Kattoum

CHAPTER 1

GENERAL INTRODUCTION

The Orientale basin (21 °S,96 °W) is the youngest and most well preserved of the lunar multi-ring basins (Hartmann & Wood, 1971). The basin consists of three concentric rings about the main cavity, known as the Inner Rook (R=230 km), Outer Rook (R=330 km), and Cordillera (R=430 km) (Figure 1.1a). The mechanism responsible for the formation of

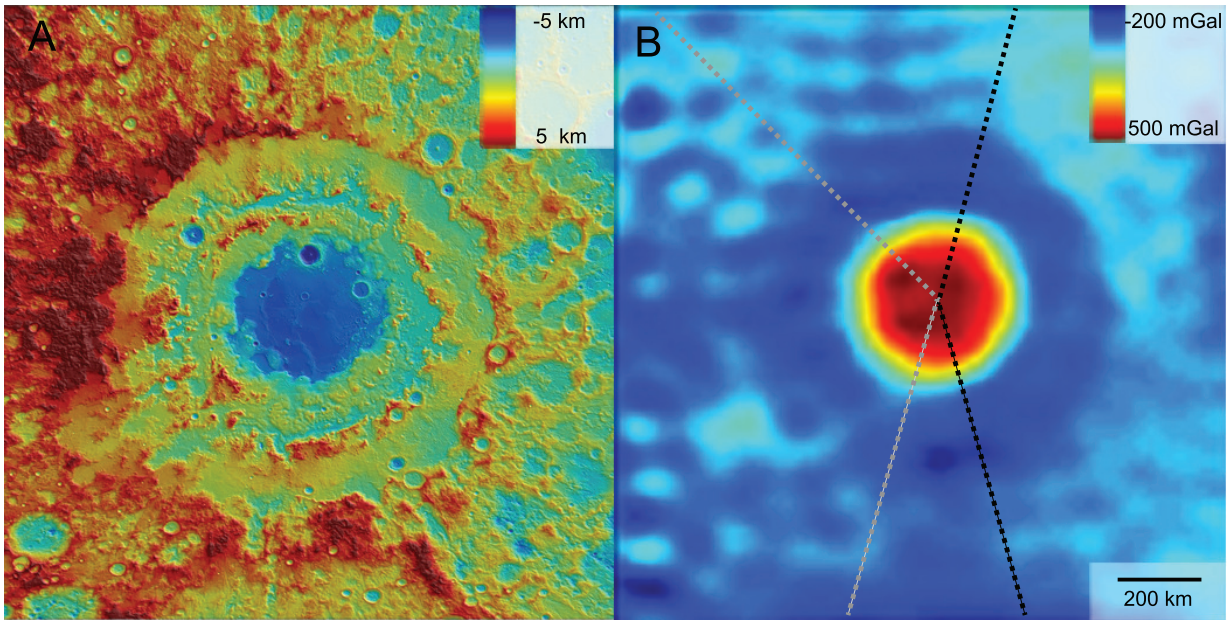

Figure 1.1: A)LOLA topography of Orientale overlain on a shade of relief map. B) Bouguer anomaly of the moon focused on the center of Orientale. Gray dashed lines encompass sector 1 and black dashed lines encompass sector 2.

the rings is not known, though several theories have been proposed (Baldwin, 1981; Head, 1974, 2010; Melosh & McKinnon, 1978; Schultz et al., 1981; Yue et al., 1990). Early on it was noted that Orientale's rings, with the exception of the Inner Rook, possessed inwardly dipping faces consistent with the morphology of fault scarps (Hartmann & Wood, 1971).

Some of the debate regarding the formation mechanism of the rings stems from the interpretation of the structure of the basins. In particular, it is not clear which of the rings

should be defined as the rim of the basin, in a manner analogous to the rims of simple or complex craters. In the following discussion, we use the term rim to refer to the ring that most closely coincides with the modified excavation cavity of the basin resulting from the collapse of the transient cavity. Other rings may have formed either interior or exterior to the rim. Understanding the position of the actual basin rim has important implications for basin formation, since this determines the size of the impact required to form the basin as well as the amount of melt and ejecta produced. Spudis et al. (1984) constrained the excavation cavity to lie within the Outer Rook ring by identifying pre-Orientale landforms within the Cordillera and parts of the Outer Rook ring that have been partially buried by Orientale ejecta. Such features included an extensive pyroclastic vent system between the Cordillera ring and the Outer Rook ring that would have been otherwise destroyed had the transient cavity expanded into this area. (Head, 2010) interprets the Outer Rook to be the rim of the excavation cavity, and the Inner Rook to be the edge of the melt zone below the point of impact. Crustal thickness models on the other hand reveal that the Inner Rook most closely coincides with the rim of the excavation cavity (Wieczorek & Phillips, 1999).

In this study, we take the approach of examining the Orientale ring structures through analysis of topography and gravity data. Previous studies used a spherical harmonic approach to directly invert the gravity and topography data for the subsurface structure of the basin (Wieczorek & Phillips, 1999). However, that approach is not effective in identifying discrete structures in the subsurface such as ring faults. Here, we instead use forward models of the gravitational signature of ring faults crossing density interfaces in the subsurface. These models are used in a Monte Carlo approach to invert for the best-fit fault parameters to match the observed signature of the rings. This work uses existing low-resolution gravity data from a series of NASA lunar orbiters (Mazarico et al., 2010) but makes predictions towards what higher resolution GRAIL gravity data (Zuber et al., 2012) may reveal in Orientale.

CHAPTER 2

BACKGROUND

Understanding the formation of multi-ring basins such as Orientale are important for gaining better knowledge towards impact cratering mechanisms and modification. It is not clear which ring of Orientale forms the actual rim of the excavation cavity. Determining the location of the rim can give information about the size of the projectile and the magnitude of the impact. Furthermore, the location of the rim of the excavation cavity can help aid in whether the rings formed during impact or whether they were a result of subsequent crater modification. Understanding the mineralogy and the subsurface crustal structure may reveal information about ring formation and basin modification.

2.1 Theories of ring formation

A number of theories have been proposed to explain the formation of ring structures around lunar basins. Baldwin (1981, 1972, 1949, 1963) explained the formation of the basin rings through a frozen tsunami model. This was supported by Dorn (1968, 1969) who showed that the spacing of the rings can be achieved from wave disturbances in a 50 km thick inviscid layer overlying a rigid layer. This implies that the rings and excavation cavity of these basins formed simultaneously Crater counts around the Altai ring of Nectaris shows significant evidence that it is younger than the basin, but the same analysis in Orientale was inclusive in determining the relative age of the Cordillera (Hartmann & Wood, 1971). The frozen tsunami theory has been supported by several recent studies (Shi et al., 2009; Yue et al., 1990), though most recent work favors tectonic mechanisms of generating the rings.

Melosh & McKinnon (1978) proposed a model with a two-layer crust that has a brittle/elastic upper layer and a weaker lower layer. An impact can drive the weaker material in the lower layer to flow inward to the cavity center causing a shear stress at the boundary of the two layers. This shear stress reaches a maximum with increasing radius eventually causing

failure as the radial stress reaches the strength of the upper elastic layer. This model successfully predicts ring formation at a distance roughly consistent with observations; however, it only produces one ring.

Another model proposed to describe the formation of the rings within Orientale and other basins is the mega-terrace model (Head, 1974). In this model, the excavation stage of the impact forms a transient cavity that is approximately the size of the Outer Rook, with deposition of ejecta outside this ring. During the modification stage, shock-melt lines the transient cavity and collects on the crater floor. The mega-terrace then forms and slumps inward forming the Cordillera ring along pre-existing structural trends, analogous to terrace formation in complex craters (Osinski & Spray, 2005). The diameter of the Outer Rook is decreased from its initial position by the inward slumping of the mega-terrace.

Head (2010) modified the mega-terrace model to the nested melt cavity model to explain ring formation. The area below the transient cavity moves down and radially outward in a region referred to as the displaced zone (Melosh, 1989; Spudis, 2005). The point of impact is also underlain by a substantial melt zone. As the size of the impact increases, the thickness of the melt zone approaches the depth of the transient cavity (Grieve & Cintala, 1992). The weak zone induced by melt inhibits central peak formation during the rebound of the transient cavity floor, causing the formation of a peak-ring rather than a central peak (Grieve & Cintala, 1992). Head (2010) interprets the Inner Rook to be the edge of the melt zone and the Outer Rook to be the rim of the excavation cavity. The Cordillera then forms from inward lateral motion along listric faults exterior to the excavation cavity (see Figure 1, Head (2010)). In this model, Orientale is interpreted as an enlarged peak-ring basin with an additional outer ring, making the Outer Rook the rim of the basin.

These models differ in their predictions for the subsurface structure of the rings. In the ring tectonic theory of Melosh & McKinnon (1978), the Inner Rook is the rim of the excavation cavity, and the Outer Rook and Cordillera are tectonic rings outside this cavity. This is consistent with crustal thickness models that equate the Inner Rook to the rim of the

excavation cavity (Wieczorek & Phillips, 1999). In contrast, the mega-terrace and nested melt cavity models interpret the Outer Rook as the rim of the excavation cavity, with the Inner Rook being the edge of the melt zone and the Cordillera being an outer tectonic ring. Thus, in this model ring faults would be predicted to only underlie the Cordillera, with the Outer Rook and Cordillera having different origins and subsurface structures. The frozen tsunami hypothesis (Baldwin, 1981) does not predict tectonic ring faults beneath any of the rings. Although these models have shown promise in explaining ring formation, they lack the use of data from Orientale to explain the observations. The interpretations presented above can be compared with the results of the inversion of the gravity data in this study.

2.2 Lunar crustal composition and structure

This study will use the gravitational expression of the rings to invert for the ring fault parameters (dip and displacement) that best match the observations. Faults generate gravity anomalies in the subsurface when they offset an interface separating two regions of differing density. Such an interface could occur either at the crust-mantle boundary or an intra-crustal interface separating materials of different density. We here review the current understanding of the interior structure of the Moon.

Apollo mission samples revealed that the oldest lunar crust was rich in plagioclase (Smith et al., 1970; Wood et al., 1970). This is explained by a global magma ocean that differentiated into an ultramafic mantle rich in pyroxene and olivine and a crust rich in plagioclase (Smith et al., 1970; Wood et al., 1970). After 70-80 % crystallization of the magma ocean, the liquidus temperature of plagioclase is reached, increasing the buoyancy of the now crystallized plagioclase, allowing it to rise to the surface (Shearer & Papike, 1999). A seismic discontinuity located at 500 km depth has been interpreted as the maximum depth of magma ocean (Nakamura, 1983). During crystallization of the magma ocean, the late-stage residual melt referred to as KREEP (Potassium, Rare Earth Elements, and Phosphorus) would concentrate between the crust and mantle (Warren & Wasson, 1979). This KREEP-rich material is concentrated on the lunar nearside (Jolliff et al., 2000; Wieczorek & Phillips, 2000). Warren

& Wasson (1979) hypothesize that this asymmetry may be due to the magma ocean first crystallizing on the far side and extruding all of the radionuclides to the nearside resulting in the gradual accumulation of KREEP.

The lunar crust has been proposed to consist of two-layers, with an upper anorthositic crust and a more noritic lower crust (Wieczorek & Phillips, 1999). This crustal stratification is supported by the Apollo seismic experiments in a four station seismic network set up by the Apollo 12, 14, 15, and 16 missions. The total crustal thickness beneath the Apollo landing sites was found to be 60 km with a 20 km thick upper crust and 40 km thick lower crust (Toksösz et al., 1974). Reanalysis of the seismic data (Khan et al., 2000) however estimated the crustal thickness to be 455 km without any evidence for a dichotomous lunar crust. Additional reprocessing of the seismic data (Lognonne et al., 2003) suggests a major discontinuity at 302.5 km depth which is interpreted as the crust/mantle transition. Other discontinuities between 15-28 km are also found, but are speculated to be impact induced fractures or a result of serial magmatism.

Although one would expect large impact events such as Orientale to have excavated out the lower noritic crust, there is no evidence for this in most basins covered by mare flood basalt since the mare obscures the mineralogy beneath. Rock types derived from multispectral data on the other hand have revealed material that is noritic in composition in South Pole-Aitken since it is not flooded with mare (Pieters et al., 2001). This noritic material was found to be pervasive both laterally and vertically and was interpreted to be impact melt/breccia deposits that originated from the lower crust. This supports the idea of a more mafic lower crust, but not necessarily the idea of a global noritic lower crust. In Orientale, anorthositic norite and noritic anorthosite were found to be the main constituents within the highlands units with the exception of the Inner Rook massifs (Spudis et al., 1984). The entire eastern Inner Rook Mountains however were found to be mainly comprised of pure anorthosite (Hawke et al., 1991, 2003; Spudis et al., 1984). Furthermore, the ejecta within Orientale is more mafic in composition than the Inner Rook Mountains, so it is speculated

that the mafic material may overlie true anorthosite (Hawke et al., 2003). Clementine and Lunar Prospector data have also been used to measure FeO concentrations in ejecta deposits of large basins to probe the lunar crust (Bussey & Spudis, 2000). These studies propose a three-layer crust that consists of a top mixed feldspathic layer that may be a few to 10's of km in thickness overlying an anorthositic layer, which in turn overlies a more magic lower crust. The lack of a mafic noritic crust exposed in the region of Orientale suggests that a thick anorthositic crust exists within the Orientale region. The division of the upper crust into feldspathic and anorthositic layers would have a minimal effect on the gravity field since the feldspathic and anorthositic crust do not have a large density contrast. Conversely, highly porous megaregolith can cause a large density contrast.

In addition to the crustal layering described above, many basins contain thick mare basalts in their interiors. Data from the Clementine LIDAR suggest that the depth-to-diameter ratios of lunar basins were found to be much smaller in basins that were flooded by maria than predicted (Williams & Zuber, 1998).The mare basalts within these basins were thought to be responsible for this shallowing and so the depth-to-diameter rations were used to infer mare thickness. In the case of Orientale, a 0.6 km mare thickness was inferred. However, viscous relaxation of the basin may lead to an overestimation in thickness estimates (Wieczorek et al., 2006). Although the mare are a significant component of the crust beneath the basin floors, the thickness of the mare within this analysis does not affect the results since our focus is in the area beneath the rings. In summary, there is significant evidence for a layered crust on the Moon, comprised of an upper crust divided into mixed feldspathic and anorthositic layers and more mafic noritic lower crust. This structure results in a significant density contrast between the upper and lower crust. In cases where faults cross this density interface, the displacements across the faults will generate gravity anomalies. Therefore, the existence of intracrustal density interface will make it possible to detect faults using gravity data.

2.3 Lunar crustal structure from gravity and topography data

Lunar crustal thickness models from the inversion of spherical harmonic gravity and topography data (Wieczorek & Phillips, 1999) have shown a thinned crust in the center of many basins as well as crustal thickening outside the basin cavity. Positive gravity anomalies arising at the center of basins such as Orientale are referred to as mascons. The positive gravity anomaly arises when the excavation cavity is partially filled by volcanics, though a number of basins have mascons in excess of what can be attributed to the mare (Neumann et al., 1996). Crustal thickening outside the basin results from ejecta emplacement on the periphery of the excavation cavity (Wieczorek & Phillips, 1999). The weight of the ejecta translates the crust downwards and has a net thickening effect. High resolution crustal thickness models of Orientale reveal inflections in the Moho beneath the ring structures that may be related to the subsurface expression of basin ring faults (Andrews-Hanna, 2012). However, spherical harmonic gravity models are not able to resolve discrete structures such as ring faults.

CHAPTER 3

METHOD

The goal of this analysis is to test whether fault signatures can be detected beneath the ring structures of Orientale using current gravity data, and if the internal structure beneath the rings can be constrained. Previous studies used spherical harmonics to examine the structure of the lunar basins (Andrews-Hanna & Stewart, 2011; Neumann et al., 1996; Wieczorek & Phillips, 1999). However, features with abrupt transitions such as faults cannot be represented in spherical harmonic crustal thickness models because of the continuous and smoothly varying nature of the spherical harmonic basis functions. Therefore, we opt for a technique in the spatial domain to model the effect of faults within Orientale. In this approach, the subsurface structure exhibits abrupt discontinuities that are a function of the assumed location, dip, and displacements on the faults and the depths of the subsurface density interfaces that they cross. These structures generate gravity anomalies that are smooth when represented at the resolution of the existing gravity data. The properties of the ring faults can then be iteratively adjusted so as to identify the parameters that are consistent with the observations. We emphasize that the interpretation of potential field data is inherently non-unique, and smoothly varying crustal models fit the data as well as models with fault-induced discontinuities. The purpose of this analysis is to use the *a priori* geological expectation of tectonic ring structures in the subsurface to guide a search for the fault properties that satisfy the data. This approach allows us to abandon the implicit assumption in spherical harmonic crustal thickness models that all density interfaces are smoothly varying, which is likely incorrect in the vicinity of the basin rings.

3.1 Data

Since the goal of this study is to constrain the internal structure of Orientale beneath its rings, the model predictions are compared to the Bouguer anomaly beneath those regions.

The Bouguer anomaly is calculated in the spherical harmonic domain (Wieczorek & Phillips, 1998) from the gravity (Mazarico et al., 2010) and topography data (Smith et al., 2010) (Figure 1.1b). The Bouguer anomaly was calculated 3 km above the surface up to degree 120 with a cosine taper from degree 100-120 to dampen high frequency noise. Degree 120 is close to the point at which the error spectrum intersects the power spectrum of the field (Mazarico et al., 2010), and so the data is expected to have a considerable contribution from noise. A density of 2700 kg/m^3 for the upper crust is chosen based on a study (Huang & Wieczorek, 2012) that uses localized spectral admittance to constrain the density of the upper crust from the most recent topography and gravity data. Degrees 2,0 and 2,2 were removed to account for rational-tidal deformation (Wieczorek & Phillips, 1998). Orientale was then isolated from the global map by averaging a set of radial profiles extending outward from the center of the basin along great circle paths with an azimuthal spacing of 3° (Figure 1.1b), which has the effect of amplifying the signal to noise ratio allowing for a higher resolution analysis (Andrews-Hanna & Stewart, 2011).

Since the signature of the rings in the Bouguer anomaly is subtle, the first horizontal derivative of the Bouguer anomaly was taken in the radial direction for both the data and the model results (commonly given in units of Eötvös, where 1E = $10^{-9}s^{-2}$). The first derivative of the gravity anomaly is commonly used in the technique of gravity gradiometry to isolate the boundaries of density contrasts as can arise at faults (Barbosa et al., 2007; Klingel et al., 1991). A three-point moving average filter was then employed to smooth out any noise arising from azimuthal averaging due to the coarse resolution of the global gravity grid. The Bouguer anomaly and its gradient (Figure 3.1b and Figure 3.1c) are plotted below a 2D cross-section of the topography of Orientale (Figure 3.1a). There, we see inflections in the Bouguer gradient that correspond to the locations of the ring structures between 250 and 500 km radius.

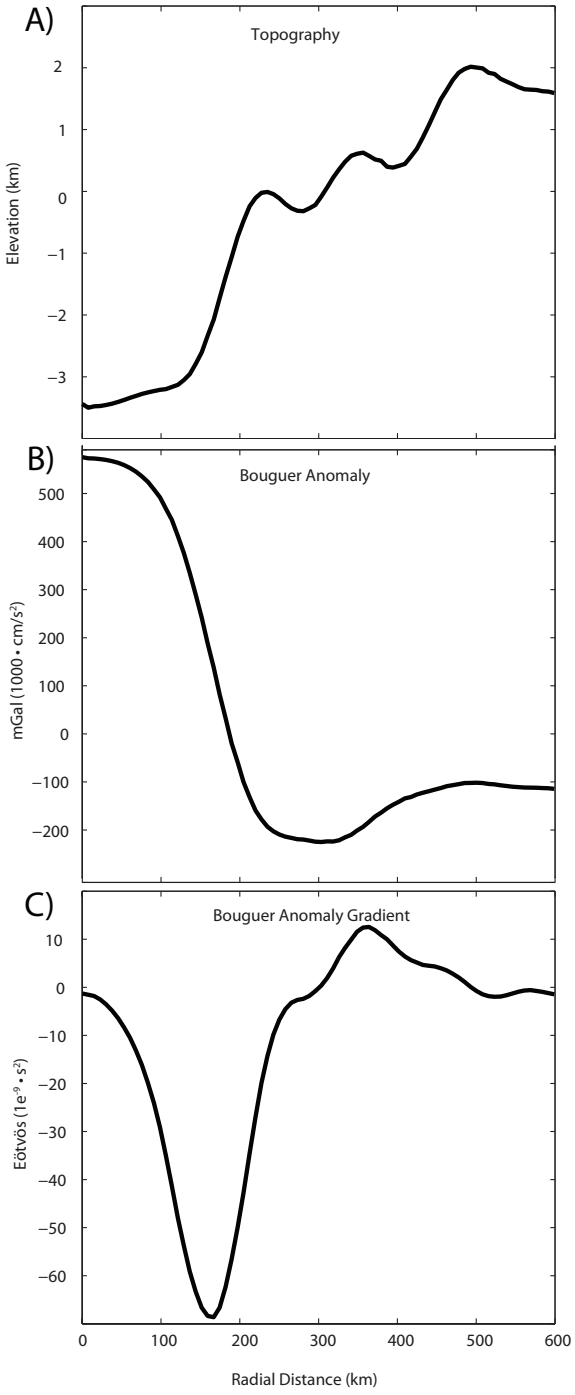

Figure 3.1: A)Azimuthally averaged topography of Orientale B) Azimuthally averaged Bouguer anomaly of Orientale. C) Gradient of azimuthally averaged Bouguer anomaly with a 3-point moving average filter applied.

3.2 3D Forward model

We began by constructing an average model in 3D representing the large-scale subsurface structure of Orientale excluding the possible effects of the ring faults. An exponential approximation of the ejecta thickness as a function of distance from the basin rim (Fassett et al., 2011) was used to account for the crustal thickening by the ejecta. This geologic representation of the ejecta thickness is to first order consistent with the results of crustal thickness models (Wieczorek & Phillips, 1999). Within the basin center, the models assume an uplifted Moho and a thinned crust, consistent with previous crustal thickness models (Wieczorek & Phillips, 1999). Beginning with this simple representation of the known long wavelength structure of Orientale, faults were then added to the model with starting points at the flanks of both the Cordillera and Outer Rook. These faults can be thought of as concentric ring faults with a sub-conical geometry. A forward approach was taken to model the gravity and test the fit between the data and model results. Several parameters were varied in the model to fit to the data, including the depth to an assumed intracrustal interface, the density contrast across that interface, the fault displacement, and the fault dip. Since some constraints exist on the density of the upper crust (Huang & Wieczorek, 2012), the density of the lower crust was varied while holding the density of the mantle and upper crust constant so as to reduce the number of free parameters. A Bayesian approach was then implemented to efficiently explore the parameter space using a Monte Carlo Markov Chain technique (Mosegaard & Tarantola, 1995; Sambridge & Mosegaard, 2002).

The models were set up in the Cartesian domain, neglecting the effect of the curvature of the surface. Despite the large size of Orientale, we find that the effect of sphericity on the gravity anomalies over the ring structures is small and does not have a significant impact on the results. The neglect of sphericity may introduce long wavelength errors in the model results, but this does not affect the results of this analysis since it focuses on shorter wavelength features associated with the rings spanning a radial distance of 180 km. Given the size of the moon (R=1738 km), sphericity will have only a minor effect on an area of

this size.

A 3D model of Orientale was created in a rectilinear square grid of approximately 1.3 million prisms (Figure 3.2). The gravity anomaly arising from each prism was calculated

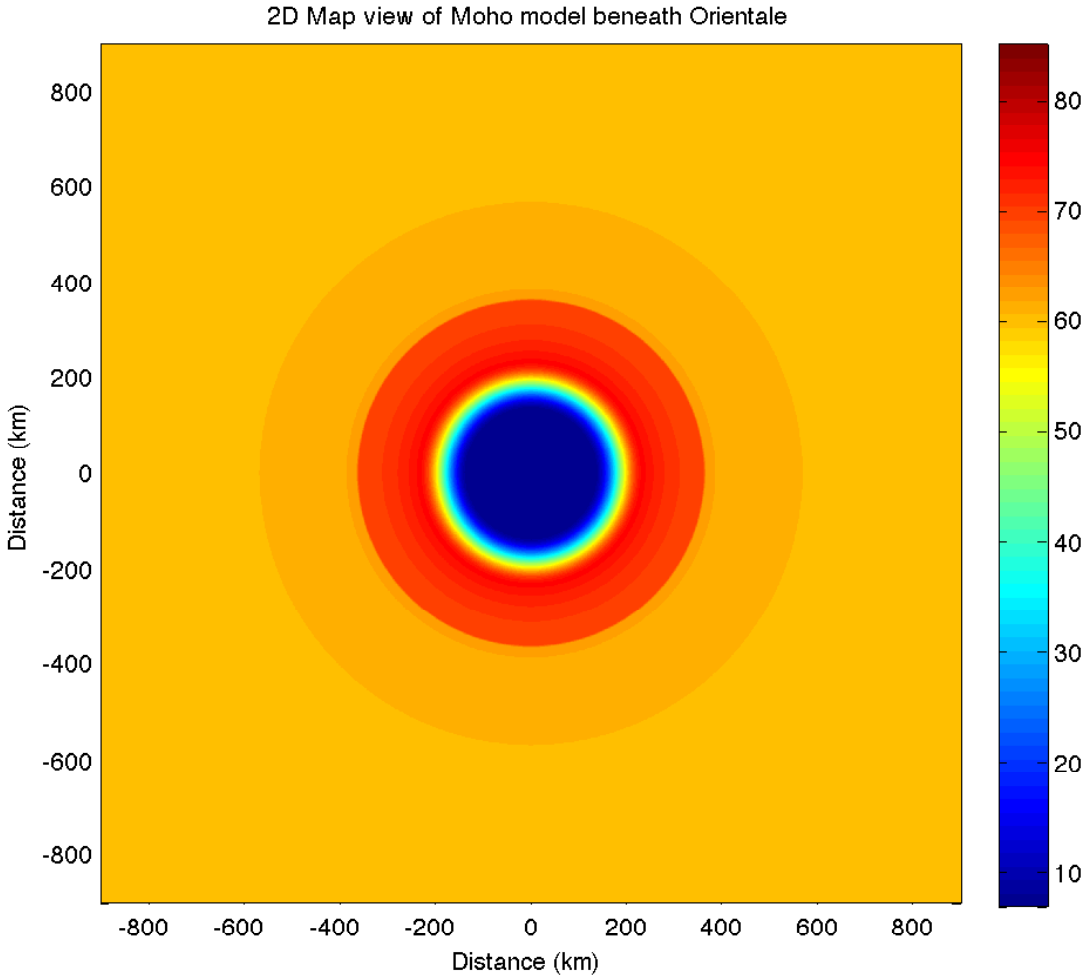

Figure 3.2: Horizontal plane through the 3D model of Orientale showing the Moho interface when viewing it from the top. Color bar is depth below the surface given in km.

following Blakely (1996) where the gravitational response of a prism measured at the origin is:

$$g = G\rho \sum_{i=1}^{2} \sum_{j=1}^{2} \sum_{k=1}^{2} u_{ijk}[z_k \arctan \frac{x_i y_j}{z_k R_{ijk}} - x_i \log (R_{ijk} + y_j) - y_j \log (R_{ijk} + x_j)] \qquad (3.1)$$

$$\text{where } R_{ijk} = \sqrt{(x_i^2 + y_j^2 + z_k^2)} \tag{3.2}$$

$$\text{and } u_{ijk} = (-1)^i(-1)^j(-1)^k \tag{3.3}$$

where x_i, y_j, and z_k are the locations of the sides of the prism. The universal gravitational constant G, and the density ρ scale the sum over all four corners of the prism to give the gravitational response at any point above the prism. At each horizontal position within the model domain, prisms extend vertically between the surface and intracrustal density interface, the intracrustal density interface and the Moho, and the Moho and set and a set maximum depth within the mantle. The 3D model was generated based on our current understanding of the large-scale structure of Orientale, including an uplifted Moho within the center of the basin (thinned crust), crustal thickening outside the excavation cavity, a dual-layered crust, and ring-faults (Figure 3.3). The average crustal thickness of the model outside of Orientale is set to 60 km, consistent with crustal thickness models of Orientale (Wieczorek & Phillips, 1999).

The gravity was calculated along a single radial profile extending from the edge of the model domain to the basin center, at an elevation of 10 km above the top of the model domain (equivalent to 3 km above the lunar surface). The symmetry of the basin relative to the observation profile allows the model domain to be limited to one half of the basin, with the gravity anomaly from each cell scaled by 2 to represent the equivalent cell on the opposite side of the basin.

The top of the intracrustal interface beneath the basin floor was set to an elevation of -5 km and the top of the Moho at -7 km, for a total crustal thickness of 3.2 km. This is somewhat greater than the crustal thickness of 0.7 km obtained by Hikida & Wieczorek (2007), but this has little influence on the results over the ring structures outside of the excavation

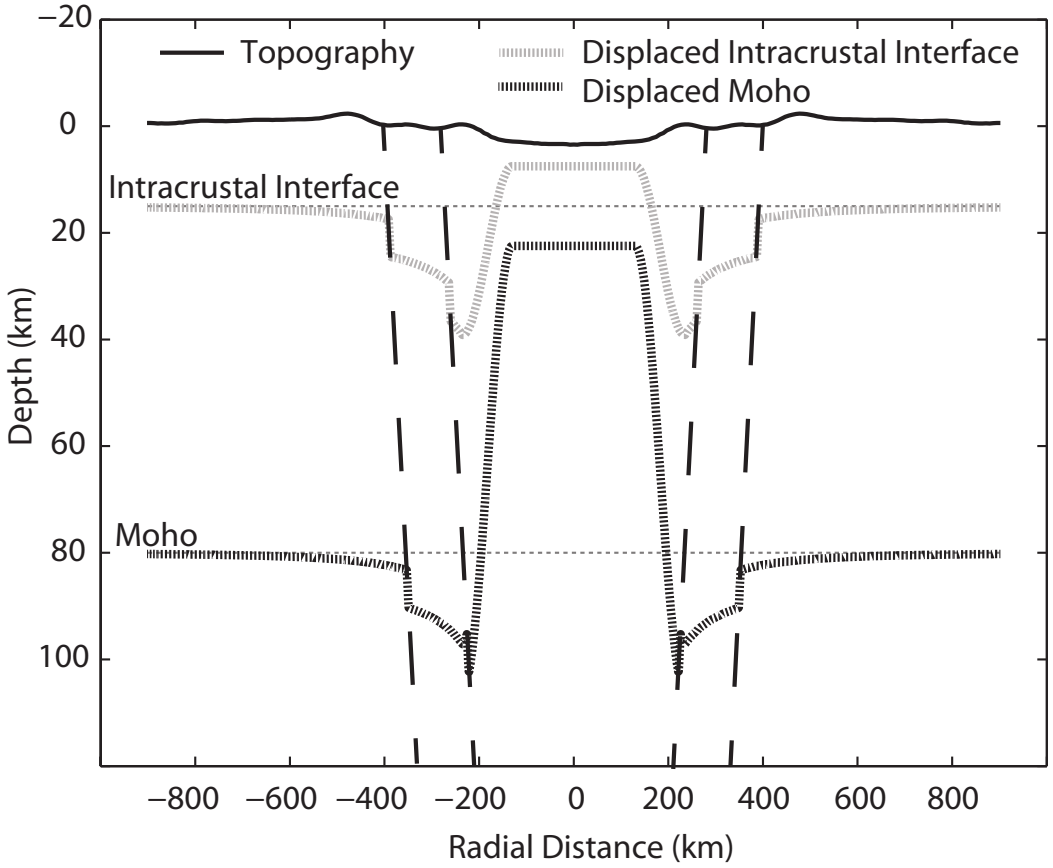

Figure 3.3: Representative cross-section of 3D model of Orientale for the case of 60 ° fault dips (dashed lines).

cavity. The edge of the top of the uplifted intracrustal interface and Moho beneath the center of the basin is set to 130 km to match the Bouguer anomaly. A cosine transition is then used to connect the top of the intracrustal interface and Moho beneath the basin center to the respective interfaces in the crustal thickening outside the basin to provide a smooth transition. This simple geometry provides a reasonable match to the data.

The ejecta thickening function adopted from Fassett et al. (2011) was used to approximate the crustal thickening beneath the rings of the basin:

$$\mathrm{t} = T_{CR}(r/R_{CR})^{-B} \tag{3.4}$$

where t is the ejecta thickness, R_{CR} is the radius of the Cordillera (465 km), T_{CR} is a scale factor that represents the thickness of the Cordillera ring ($T_{CR} = 2900 \pm 300m$), and B is the power-law exponent (2.8). This function was based on observations beginning at the Outer Rook which showed an exponential decay in ejecta thickness moving radially outward. The ejecta thickening was applied to the upper crust spanning radii between the Inner Rook at 235 km and the end of the model domain at 900 km, at which point it has decayed to the average crustal thickness of 60 km. We adopt a scale factor for T_{CR} of 1100 m. Though this is lower than the range given in Fassett et al. (2011), with the addition of faults, this value provides a better overall fit to the gravity data.

The model was set up to represent circumferential ring-faults crossing the density interfaces at the intra-crustal density interface and Moho. The prisms in the model have horizontal dimensions of 1 km, and vertical dimensions spanning between the model interfaces. This prism size is considerably smaller than the resolution of the data, but this has no effect on the model results since the predicted gravity is calculated on an observation plane with the same height and resolution as the data. This fine grid spacing is necessary in order to adequately sample the range of possible values of fault dip and displacement. The faults intersect the surface at the base of the Cordillera and the Outer Rook.To compare the model predictions with the data, the spatial domain result was expanded into the spherical har-

monic domain and underwent the same processing and filtering as the data. The azimuthal average of the model result was taken and then the gradient was calculated in the radial direction. The root-mean-square (RMS) misfit was calculated between the model result and the data between radii of 250 and 432 km after removing a first-order polynomial fit to both the model and data to take out any long wavelength effects arising from inaccuracies in the assumed pre-faulting basin structure. This radius range encompasses the subsurface expression of the Outer Rook and Cordillera rings, but excludes the Inner Rook and the topographic peak of the Cordillera.

Several scenarios were tested to examine the basin structure. We began with a model in which both the Outer rook and Cordillera are underlain by ring faults, with identical displacement and fault dip.There is disagreement over whether the Outer Rook represents the basin rim (Head, 2010) or a ring structure external to the rim (Wieczorek & Phillips, 1999), so a model with only the Cordillera ring fault was examined. Furthermore, it is possible that the faults terminate within the lower crust after transitioning to listric faults, so models with no fault offsets across the Moho were examined as well. Models without an intracrustal interface were also tested since the existence of an intracrustal interface is debated. Although, the azimuthal average of the gravity data was calculated to dampen high frequency noise, Orientale is not perfectly symmetric. Hence, different sectoral averages of the basin are taken based on systematic variations in the Bouguer anomaly from one part of the basin to the other.

3.3 Inversion

A Bayesian approach was taken to invert for the free parameters left within the model: the fault dip, the fault displacement, the depth to the intracrustal density interface separating the upper and lower rust, and the density contrast across that interface. A Markov Chain Monte Carlo method (MCMC) (Mosegaard & Tarantola, 1995; Sambridge & Mosegaard, 2002) was adopted to find a suitable range of parameter space to fit the data. Several different types of MCMC algorithms exist. In this analysis, we find that a standard MCMC

approach of perturbing the model parameters until convergence is reach is most suitable for our problem because of the simplicity in its implementation and its rapid convergence. The MCMC algorithm works through a random walk through the parameter space where different posterior states are visited by perturbations to the model parameters (Mosegaard & Tarantola, 1995). Each new model tested in the random walk is dependent on the previous model. The dependence between the new and old model in the MCMC algorithm cause the chain to remain in regions of higher probability. This memory mechanism of the MCMC technique is responsible for improved efficiency in relation to simple Monte Carlo methods (Woodruff et al., 2010).

The objective function, which is some measure of misfit between the model predictions and the observations, is utilized to evaluate the models being tested and to monitor the convergence. One of the strengths of MCMC approaches is that they work by directly sampling a parameter space without relying on the objective function being smooth. Although different measures of misfit can be used, linear problems typically use quadratic functions which lead to a least squares technique and an ellipsoidal objective function in the parameter space (Sambridge & Mosegaard, 2002). In this case, the forward model equation (3.1) is linear, so we adopt the root mean square (RMS) misfit between the model and the data.

The algorithm began at a randomly chosen point in the four-dimensional parameter space (dip, displacement, interface depth, and density contrast). The data RMS misfit, $\phi(m)$, was calculated over the region of interest beneath the rings, between 250-432 km radius. This range avoids the influence of the gravity arising from the mascon, which would overwhelm any signatures of the ring faults. The results of the model for the new set of parameters were then tested to calculate the misfit. Each new model tested was accepted or rejected based on the misfit. Some variances in the acceptance rule can be implemented to accept less likely models (Mosegaard & Tarantola, 1995), though this was not implemented here as it was not found to improve the model performance. Although accepting less likely solutions is useful for creating the posterior density distribution after convergence is reached, it impairs

the ability of the algorithm to identify local and global minima. Using the above algorithm, convergence on a best-fit model was reached within 200 iterations in most cases.

The next set of parameters to be tested were chosen randomly from a normally distributed set of values around the most recently accepted model (Mosegaard & Tarantola, 1995). This is beneficial in that it allows the algorithm to make occasional larger steps that can allow it to get out of small local minima in the misfit. This normal distribution was set to have a standard deviation of 0.02 of the full range considered for each parameter. This choice was found to provide the optimal balance between rapid convergence and fine sampling of the parameter space. Each Markov Chain tested a total of 400 models, which was found to provide adequate convergence on a best-fit solution. Although 400 iterations were allowed, convergence was was reached within 200 iterations in most cases, as determined by a leveling out in the objective function. Multiple Markov Chains were implemented from different random initial starting points in order to ensure that the model did not get caught in a local minimum that did not provide an adequate fit to the data, and to characterize the range of solutions that do fit the data. A total of 50 MCMC implementations were performed for the full basin azimuthal average with both Cordillera and Outer Rook ring faults, while 20 implementations were performed for all other models.

Ranges of density for the lower crust were chosen to be anywhere from 2900-3300 kg/m^3, spanning the range of previous estimates of the lower crustal density (Wieczorek & Phillips, 1997) and recent measurements of the density of anorthositic norite samples from the Moon (Kiefer et al., 2012). The depth to the intracrustal interface was chosen to range between 7.5-35 km. This range is consistent with the early interpretation of the Apollo seismic experiments that identified a seismic discontinuity at 20 km depth (Toksösz et al., 1974), and the increase in density in a transition zone between 15-28 km depth in recent inversions of the seismic data (Lognonne et al., 2003). The intracrustal interface was allowed to go deeper in preliminary investigations, but resulted in the model becoming trapped in local minima that did not match the data. The vertical component of the fault displacement was

varied between 0-15 km, which is sufficient to encompass the range of observed relief in the rings. The maximum vertical offset in the rings is observed to be in the vicinity of 5 km, but this may underestimate the true fault displacement due to post-impact modification. Finally, fault dip was varied between 20-80 ° to encompass the range associated with normal and listric normal faults observed on Earth of 30-70 ° (Scholz, 2002).

After the best-fit solution was obtained from the MCMC, a simple Monte Carlo approach with random independent sampling of the parameter space was used to place bounds on the acceptable range in parameter space. The uncertainty in the observed Bouguer gradient profile was calculated from a 1-σ clone field generated from the co-variance matrix of the gravity model (provided by Erwan Mazarico, personal communication). This clone field was generated by taking the covariance matrix of the spherical harmonic gravity coefficients, diagonalizing it, and adding the eigenvectors scaled by the eigenvalues as well as a random factor (provided by Erwan Mazarico, personal communication). The azimuthal average of the clone field was then subtracted from the data to give the noise within the data. The RMS misfit between the original data profile and the clone field profile was used as the threshold misfit between the model and the data to define the 1-σ range in acceptable parameter space. The RMS misfit obtained between the data and the 1-σ was 0.831 Eötvös. Finally, in order to visualize the behavior of the model misfit as a function of the parameters, we examined 2D cross sections of the model space (e.g., fault displacement vs fault dip) centered on the best-fit solution.

CHAPTER 4

RESULTS

Of the several scenarios tested, we find that many of the solutions between the different scenarios had similar results. Furthermore, the best-fit solutions between the multiple inversions run for each individual scenario yielded similar results as well. On rare occasions, there were occurrences in where the model fell in a local minimum. The results for each scenario are presented with plots of the best-fit model and the ranges in parameters the best-fit solutions achieved. An uncertainty analysis is performed for the single full azimuthal average case. Finally, the RMS misfit for the best-fit model is discussed and a range for the RMS misfit is given for the best-fit models within each scenario.

4.1 Azimuthal average model

We first focus on the results of 50 implementations of the MCMC algorithm using the full azimuthal averages of the basin. The results are presented as scatter plots of the best-fit solutions from the multiple implementations of the Markov Chain algorithm between the parameters that are most closely related (interface depth vs density contrast, and fault dip vs fault displacement). Although the full azimuthal average results generally yielded two clusters of solutions, there is not a clear distinction between the clusters since some solutions fall in between (Figure 4.1a and b). These clusters are shown by different colors in Figure 4.1 in order to illustrate the connection between the depth-density contrast and dip-displacement relationships. The RMS misfit for all the solutions for this case range between 0.215 and 0.264 Eötvös. Solutions with RMS misfits at the lower end of this range existed within both of the clusters outlined in Figure 4.1. There is a linear relationship observed between interface depth and density contrast (Figure 4.1a and b). Cluster 1 has a range of 8.5-12.8 km for the intracrustal interface, a density contrast of 255-404 kg/m^3 between the upper and lower crust, a vertical component of fault displacement of 7.1-10.3 km, and a fault dip of

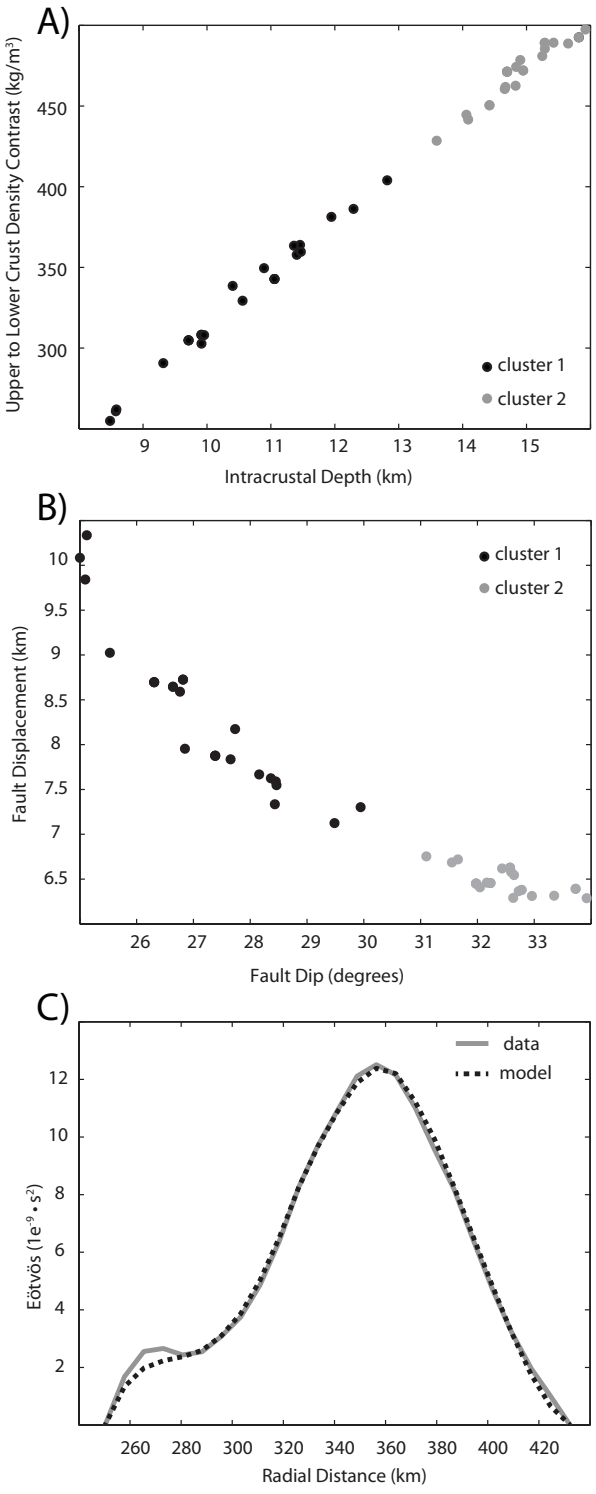

Figure 4.1: Best-fit parameter solutions obtained from multiple Monte Carlo Markov Chain runs for full azimuthally averaged basin. RMS misfit ranges from 0.215 to 0.264 Eötvös. A)Density contrast across intracrustal interface vs. intracrustal interface depth. B)Vertical fault displacement vs. fault dip. C) Best-fit model from all models ran.

25.0-29.9°. Cluster 2 has a deeper intracrustal interface depth ranging between 13.6 and 15.9 km, a higher density ranging from 428-497 kg/m^3, smaller fault displacements of 6.3-6.8 km, and slightly steeper dips of 31.1-33.9°. Histograms constructed from the parameters of the 50 best-fit solutions suggest a bimodal distribution in fault dip and the density contrast between the upper and lower crust (Figure 4.2). In this figure, the bimodal distribution however is not as obvious in the intracrustal interface depth and fault displacement parameters. The

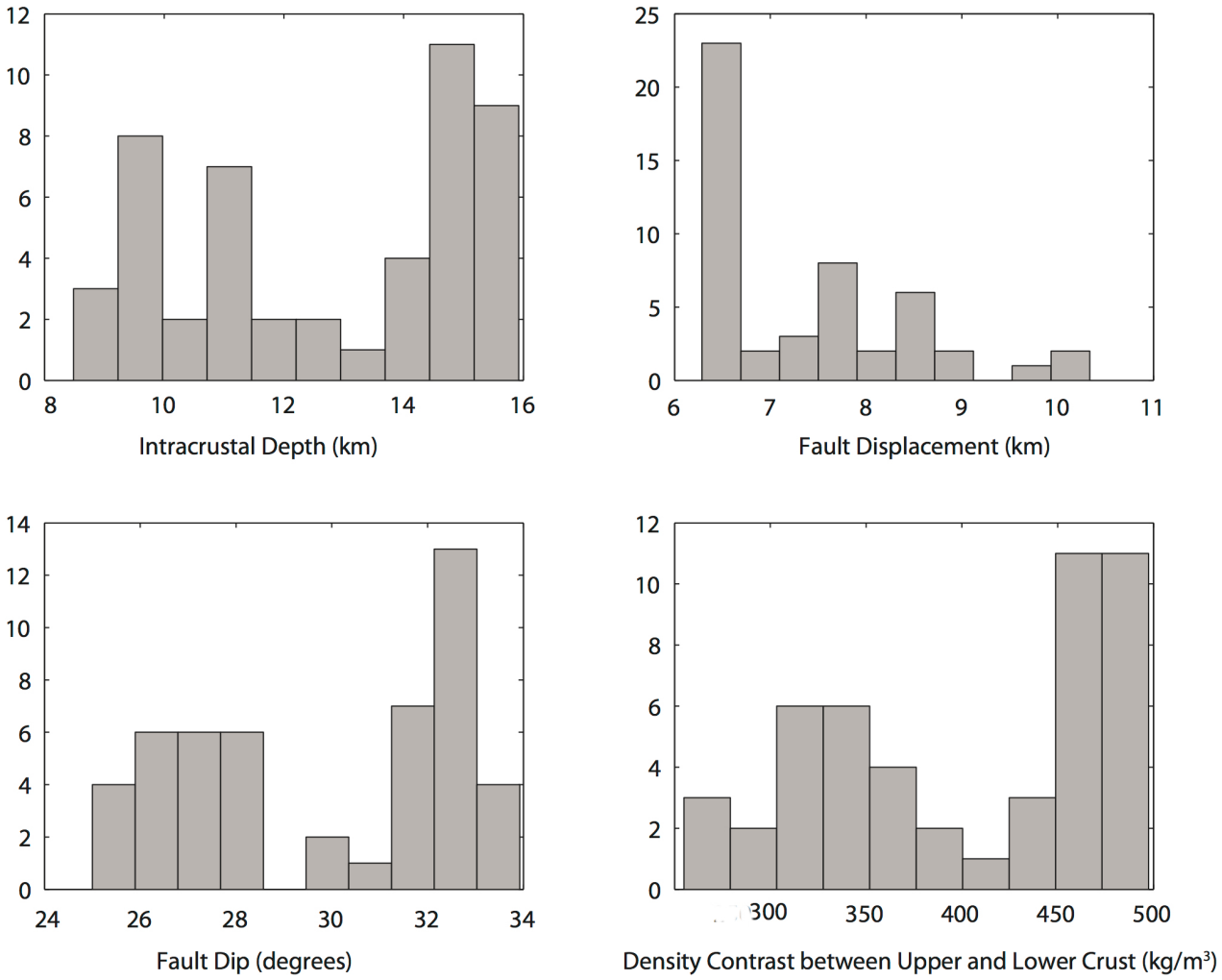

Figure 4.2: Histogram for the best-fit solutions from the 50 model runs in the Azimuthal average model case showing all parameters.

best-fit solution with lowest misfit value (ϕ = 0.215 Eötvös) has an intracrustal interface depth of 10.8 km, a vertical component of fault displacement of 7.8 km, a density contrast

of 350 kg/m^3 between the upper and lower crust giving the lower crust a density of 3050 kg/m^3, and a fault dip of 28° (Figure 4.1c). The convergence of the best-fit solution is reached within approximately 200 iterations (Figure 4.3). The tradeoffs in the parameters

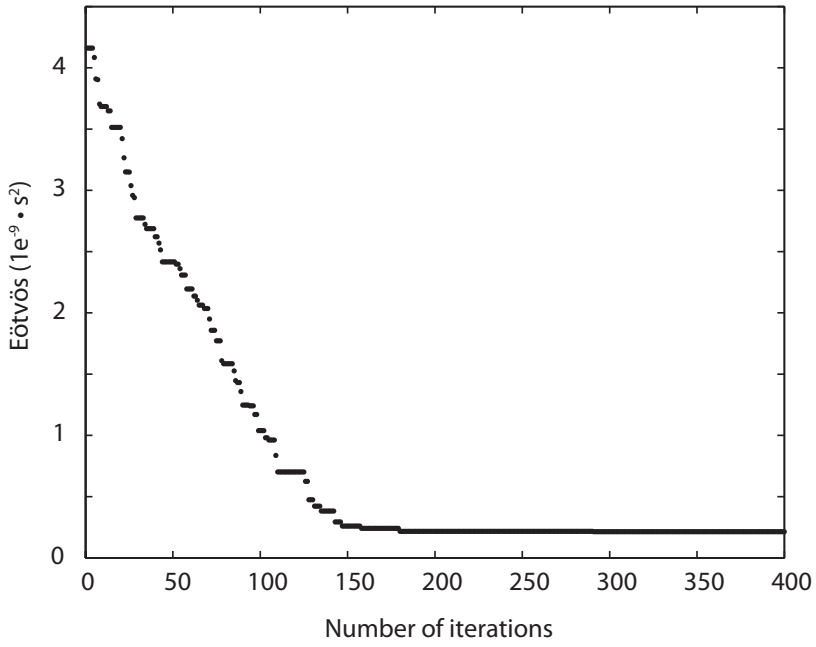

Figure 4.3: RMS misfit plotted against iteration number showing the convergence of the best-fit solution in a MCMC run for the case of the full azimuthal average model.

between the two groups are expected, since the effects of the fault displacement, the density contrast between upper and lower crust, the depth of the intracrustal interface, and dip are correlated. For example, as fault displacement increases, the solution needs a lesser density contrast between upper and lower crust and a shallower interface to match the data. Similarly, as the depth of the intracrustal interface becomes shallower, a more gentle dip is required to match the horizontal location of the gravity inflections.

Considering the range of parameter space that is acceptable at the 1-σ level based on the clone field misfit (0.831 Eötvös), intracrustal interface depths ranging from 7.5-19.8 km are allowed. Fault displacement of 5.3-12.4 km and dips of 21-42° are also within the 1-σ level. Finally, the allowable density contrast ranges from 201 to 500 kg/m^3. Histograms for these ranges of parameters show the distribution of the parameters below the 1-σ level (Figure 4.4).

Although these results are not very tightly constrained within the 1-σ level, they provide

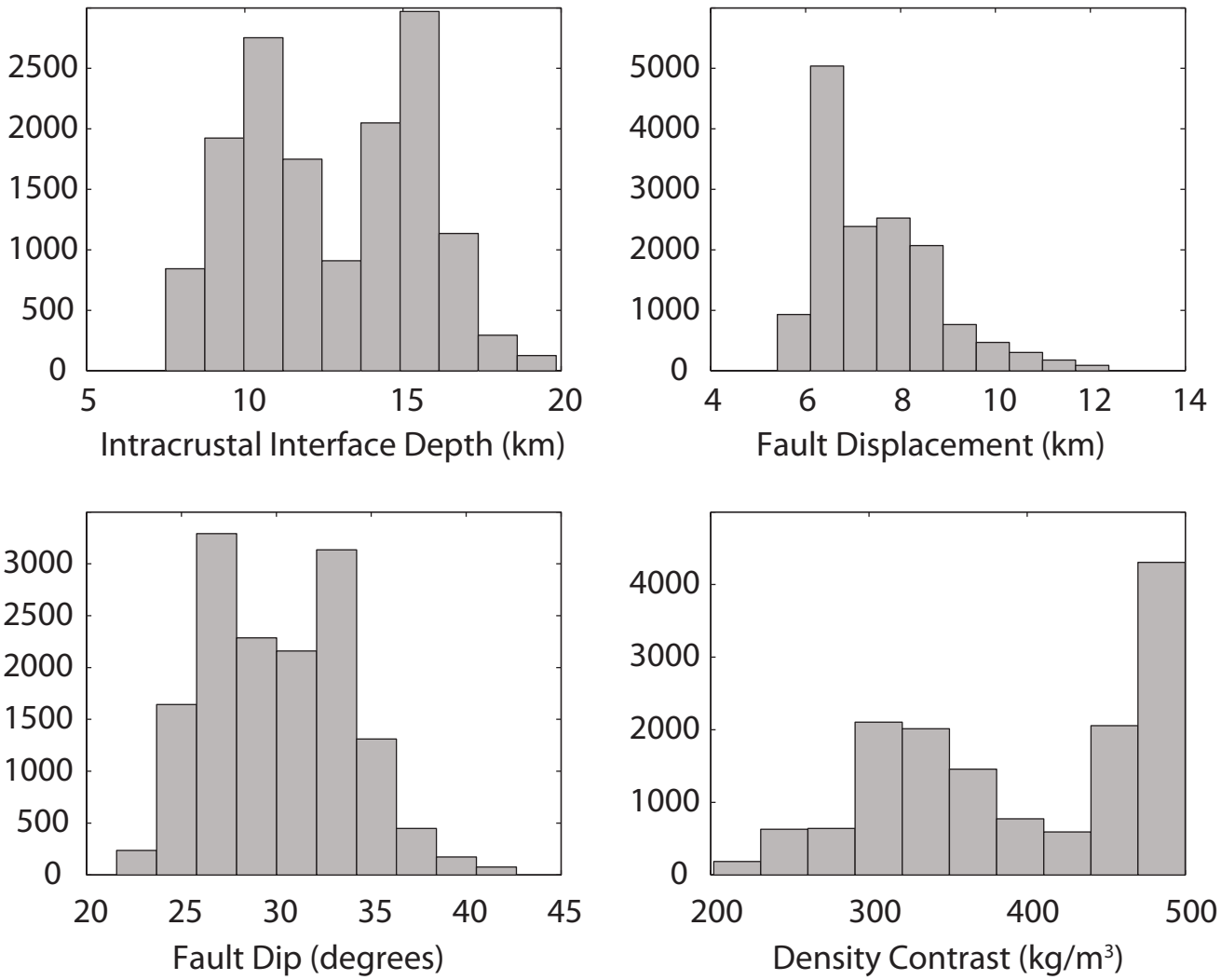

Figure 4.4: Histogram from the parameters visited in the 50 model runs from the azimuthal average model case that fall within the 1-σ error range.

reasonable solutions based on the prior geologic information. However, the model favors fault displacements at the high end of the expected values based on the observed fault scarps, and dips at the low end of the typical range for normal faults.

The 2D cross sections of the RMS misfit take slices of the misfit along orthogonal planes in the 4D parameter space, passing through the best-fit solution. This allows a visualization of the dependency of the misfit on the different parameters, which cannot be illustrated in the full four-dimensional parameter space. These cross sections show that the minimum has

a smooth and broad geometry that can encompass a diverse range of solutions Figure 4.5. The elongations of the lows in these cross sections reveal the expected parameter tradeoffs between the density contrast and the fault displacement, the interface depth and the density contrast, and the interface depth and fault dip.

4.1.1 Model with no faults crossing the Moho

In order to test, the possibility of listric faults or faults that simply terminate within the lower crust, the perturbations to the Moho from the faults were removed. Intuitively, one would expect that the inflections at the Moho provide an insignificant contribution to the final result because the decay of gravity is proportional to the square of the distance to the source of the anomaly ($1/R^2$). Furthermore, the decay in gravity gradiometry is even more rapid ($1/R^3$) and so fault inflections in the Moho should only weakly affect the data.

Once again two clusters of solutions exist in the final models from each MCMC implementation (Figure 4.6a and b). Although the clustering of solutions is stronger than that observed in Figure 4.1, there is again a linear trade-off between correlated parameters. For cluster 1, the intracrustal interface depth ranges from 7.7-11.0 km, with a density contrast of 278-349 kg/m^3. The vertical component of fault displacement spans between 7.1-7.8 km, with gentle fault dips of 23.6-28 °. Cluster 2 has deeper intracrustal interface depths ranging from 13.4-16.9 km and a higher density contrast, ranging between 410-499 kg/m^3. Cluster 2 has faults with vertical displacements between 6.4-6.9 km and dips ranging from 30.9-35.3 °. In this case a bimodal distribution is observed in all of the parameters of the best-fit models (Figure 4.7). The RMS misfit for all the solutions for this case of no faults crossing the Moho ranges between 0.239 and 0.273 Eötvös. This range differs only slightly from the case of the full azimuthal average model with faults crossing the Moho. In particular, this model favors smaller fault displacements (6.4-7.8 km) than the model with faults crossing the Moho (6.3-10.3 km). This shows that faults offsetting the Moho do have some effect on the final result. The best-fit solution ($\phi = 0.239$ Eötvös) obtained from not including faults intersecting the Moho had an intracrustal interface depth of 9.9 km, a fault-displacement of 7.3 km, a density

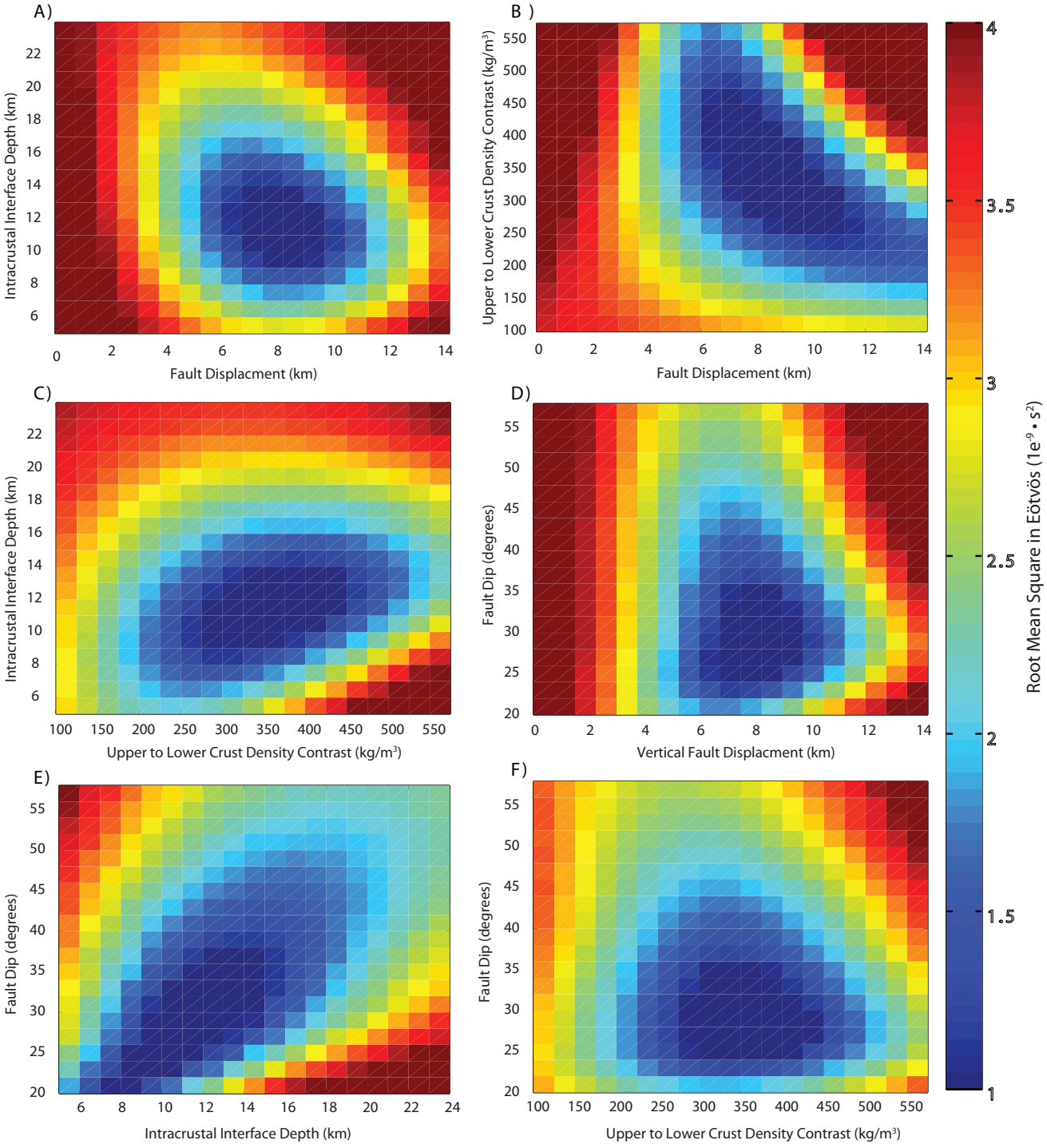

Figure 4.5: 2D cross-sections of the RMS misfit from varying two parameters at a time while holding other parameters to the value of the best-fit solution obtained from the model case including a Cordillera and Outer fault protruding down to the Moho.

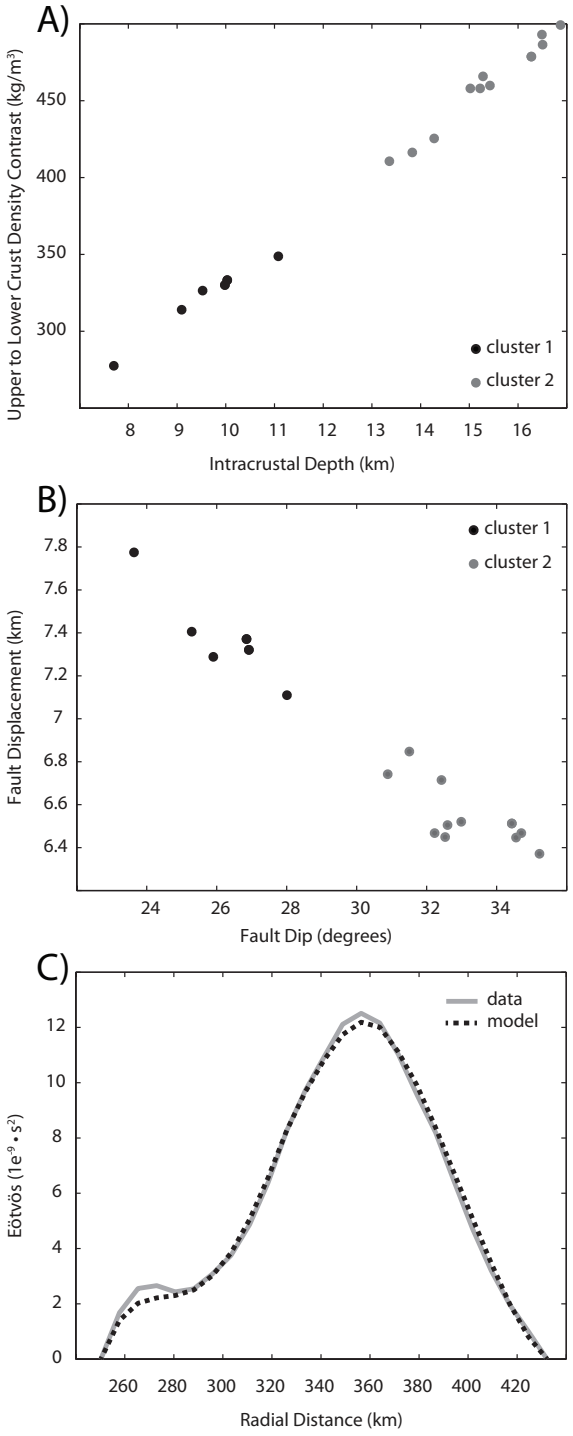

Figure 4.6: Best-fit parameter solutions obtained from multiple Monte Carlo Markov Chain runs for full azimuthally averaged basin with no faults intersecting Moho. RMS misfit ranges from 0.239 to 0.273 Eötvös. A) Density contrast across intracrustal interface vs. intracrustal interface depth. B) Vertical fault displacement vs. fault dip. C) Best-fit model from all models ran.

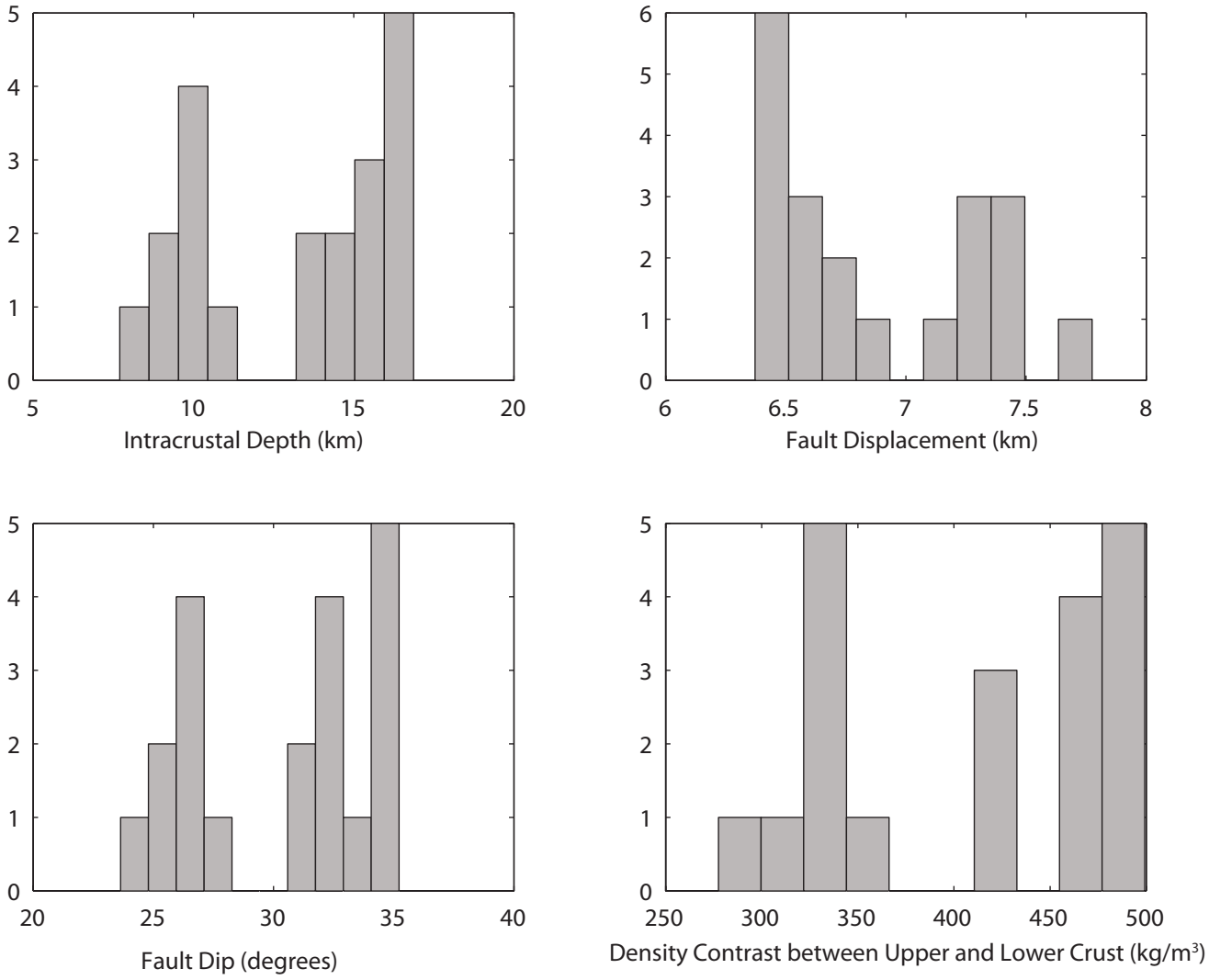

Figure 4.7: Histogram for the parameters of the best-fit solutions in the 20 models run in the case of no faults crossing the Moho

contrast of 330 kg/m^3 between the upper and lower crust, and fault dips of27° (Figure 4.6c). This best-fit solution is similar to that from the model with faults crossing the Moho, and both models provide comparable fits to the data. The range of model solutions in this case that fell below the 1-σ error level within the data had intracrustal interface depth ranges of 7.6-20.9 km, fault displacements between 5.5-9.0 km, dips of 21-44.8°, and densities of 275-500 kg/m^3.

4.1.2 Model with no Outer Rook fault

Another case that was examined is the possibility of not having an Outer Rook fault. One of the difficulties with detecting the Outer Rook fault in the gravity is that the resulting inflection is close to the edge of the excavation cavity, so its effects may be masked by the large anomaly within the center of the basin. Higher resolution gravity may better reveal the gravitational effects of the gravity anomaly arising from the Outer Rook fault.

Results with only a Cordillera fault differed from the previous results in that there was not a clear linear trend observed (Figure 4.8a and b). Although there again seems to be two clusters of solutions, the model more commonly converges on one of the clusters. The density contrast across all solutions ranged between 314-500 kg/m^3. The intracrustal interface depth has a range 7.6-16.5 km, similar to the previous results. The vertical fault displacements are on the low side, ranging between 4.5-7.4 km. Fault dip ranges between 21-35°, but the model more commonly arrived at lower dips (Figure 4.9). The solutions within these models have the lowest RMS misfit in relation to the previous models, ranging between 0.168 and 0.260 Eötvös. The two clusters may suggest that there are two minima. Alternatively, a single elongated minimum may be more densely sampled by the algorithm at its ends as the Markov Chain converges on the best-fit solution. The best fit model solution (ϕ = 0.168 Eötvös) obtained from this case has an intracrustal interface depth of 8.3 km, a fault displacement of 4.5 km, a density contrast of 493 kg/m^3, and fault dip of 22° (Figure 4.8c). Although there is not a large difference in the parameters obtained for this case, the model favors a higher density contrast and lower fault displacement. This best-fit model provides a

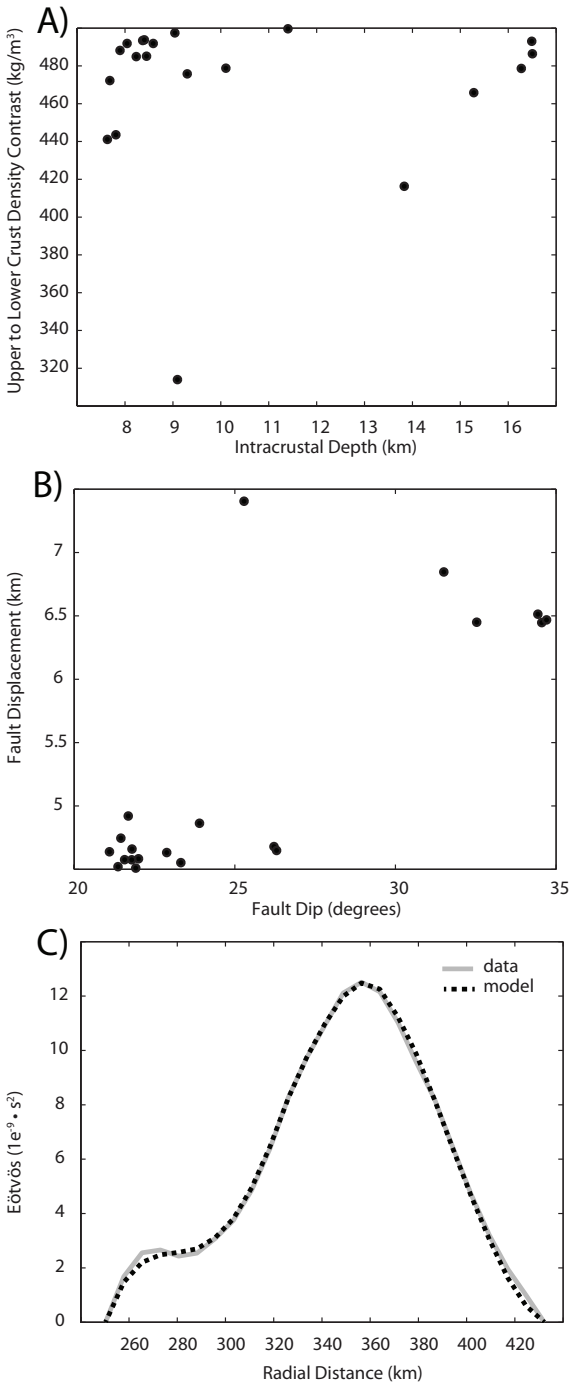

Figure 4.8: Best-fit parameter solutions obtained from multiple Monte Carlo Markov Chain runs for full azimuthally averaged basin with no Outer Rook fault. RMS misfit ranges from 0.168 to 0.260 Eötvös. A) Density contrast across intracrustal interface vs. intracrustal interface depth. B) Vertical fault displacement vs. fault dip. C) Best-fit model from all models ran.

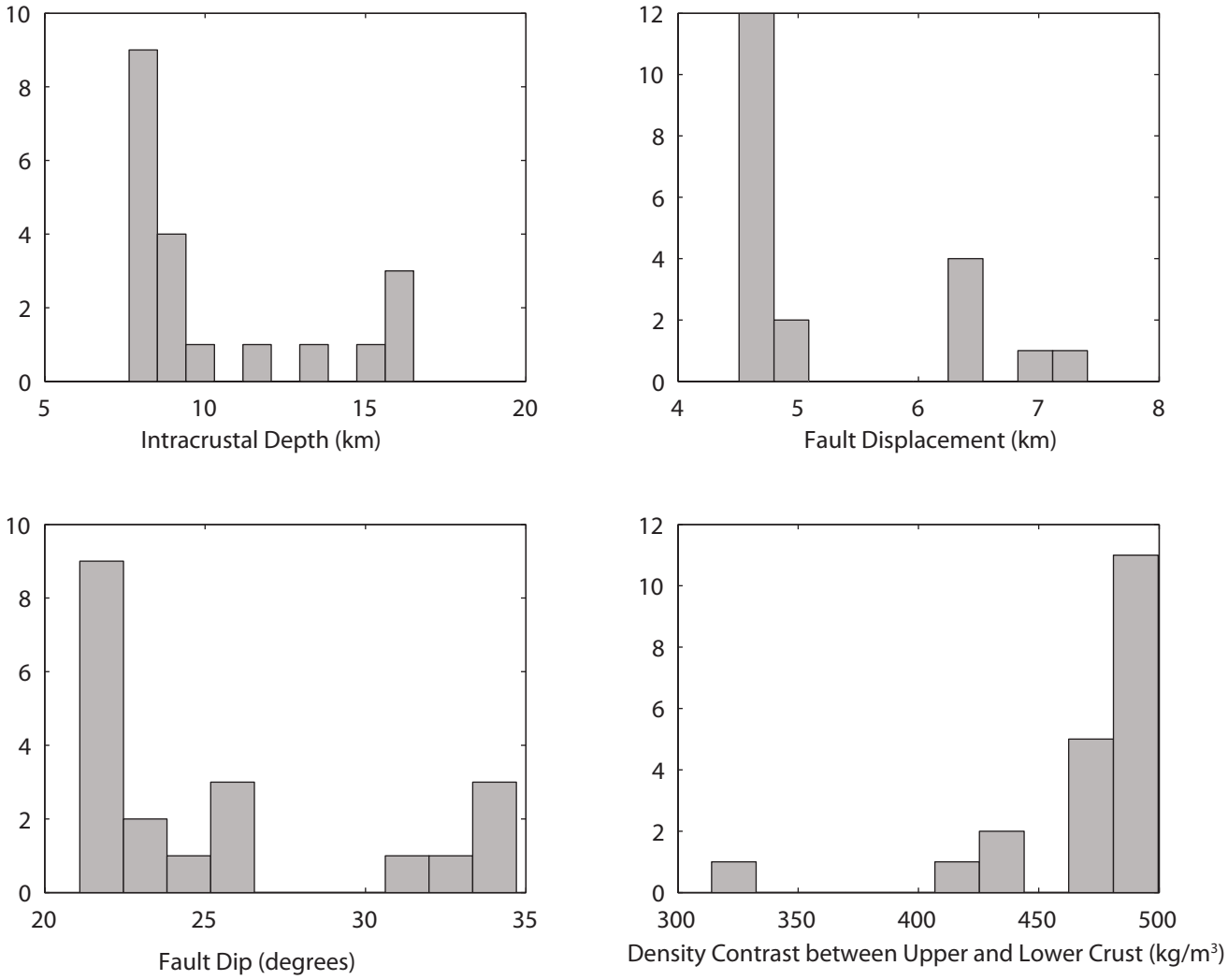

Figure 4.9: Histogram for the parameters of the best-fit solutions in the 20 models run in the case of no Outer Rook fault present.

similar match to the data. Although the scenario tested here yielded the lowest RMS misfit, it does not mean that this model is more representative of the real solution than the other models. The RMS misfits achieved in this model and all other models tested are well below the 1-σ error level discussed above. Therefore, no particular solution can be favored more than the other if they fall within the error in the data. The range of model solutions in this case that fell below the 1-σ error level within the data had intracrustal interface depth ranges of 7.6-20 km, fault displacements between 3.8-8.5 km, dips of 20-40.1 °, and densities of 300-500 kg/m^3.

4.2 Other models: no intra-crustal interface or no faults

One important test in this analysis was to examine whether a fit to the data can be achieved with a single layer crust lacking an intracrustal interface. As mentioned earlier, the decay of gravity with distance will make it difficult to detect anomalies arising at the depth of the Moho (60 km). An MCMC routine was run to solve for fault dip and displacement while holding the density contrast between the crust and mantle at 700 kg/m^3 and the depth of the Moho at 60 km. Fault dip and displacement were varied within the same range as the previous model runs, but no reasonable fit to data was achieved after 35 MCMC runs (Figure 4.10). The best-fit solution had a fault displacement of 4.2 km and dip of 20 °, but provided a very poor fit in comparison to the earlier results.

None of the previous cases run converged to a solution with 0 km fault displacement, suggesting that cases without faults provide a poor fit to the data. This was explicitly tested by examining a model with no faults. A case with an intracrustal interface at a depth of 10 km, and a density contrast of 400 kg/m^3 between upper and lower crust was run to illustrate the gradient of the model results with no faults. The results of this model also provided a poor fit to the data (Figure 4.10). Thus, the observed gravity cannot be explained by a model with a simple exponential decrease in ejecta thickness without the added effect of faults offsetting density interfaces in the subsurface. This does not preclude the possibility that the variations in the ejecta thickness and crustal structure could have mimicked the

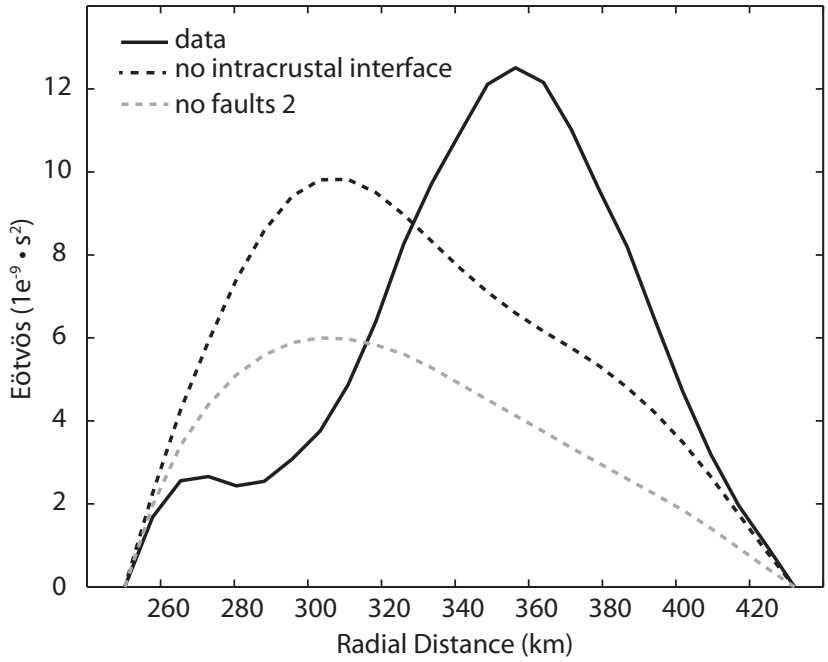

Figure 4.10: Data compared to model with no intracrustal interface and to model with no faults

effects of faults in the subsurface, but such a scenario seems unlikely.

4.3 Models of sectoral averages

Finally, sectoral averages spanning portions of the basin were examined to test if there are any differences in structure from one part of the basin to other. Since the gravity data utilized in this analysis is relatively low resolution, the sectoral models do not benefit as much from the amplification of the signal to noise ratio as the full azimuthal models. Conversely, although the full azimuthal averages may have a higher to signal to noise ratio, they may be averaging over real differences from one part of the basin to the other.

The first sector was chosen between 105-225 $^\circ$ (Figure 1.1b) of the basin where 0 $^\circ$ is defined as the radial profile extending due east from the basin center, and angle increases clockwise. This sector was chosen because of the consistency of the Bouguer anomaly within this region, with a lower Bouguer anomaly than that in the other sector. New starting points for the faults were chosen based on the corresponding topography of this particular sector.

The results obtained from sector 1 are broadly similar to the previous results. The vertical component of fault displacement shows a similar range, with displacements between of 8.4-10.5 km. The intracrustal interface depth remains at a shallower level, ranging between 9.4-11.6 km (Figure 4.11a and b). The results again show a linear correlation between fault dip and fault displacement, but the correlation between the intracrustal interface depth and density is non-linear in contrast to the previous cases. Density contrasts in this case ranged between 225-480 kg/m^3 and dips are between 24-31°. The best-fit solution (ϕ = 0.604 Eötvös) obtained from the sector 1 data has an intracrustal interface depth of 9.9 km, a fault displacement of 8.5 km, a density contrast of kg/m^3, and a fault dip of 24° (Figure 4.11c). The histograms of the parameters from the best-fit solutions from this case are shown in Figure 4.12. This solution does not provide as close of a match to the data as was found in previous models. Here the RMS misfit for all solutions tested ranges from 0.604 to 0.757 Eötvös. This is significantly larger than the misfits in the cases above but still falls within the error of the data (0.831 Eötvös). This large mismatch may be due to either the inadequacy of the model assumptions for this part of the basin, the greater noise in the sectorally averaged gravity due to averaging over fewer data points, or competing effects such as density anomalies within the crust. The range of model solutions in this case that fell below the 1-σ error level within the data had intracrustal interface depth ranges of 7.9-13.6 km, fault displacements between 7.6-11.3 km, dips of 20-31.4°, and densities of 183-500 kg/m^3.

Sector 2, encompassing the azimuths opposite to sector 1 (Figure 1.1b), does not show a simple correlation between parameters and differs most from all the previous cases (Figure 4.13). In particular, much larger fault displacements, ranging form 13.1-14.9 km, are needed to match the data. The solutions obtained for the other parameters, however, are similar to the previous cases. The intracrustal interface depth remains at a shallow level (7.5-11.2 km), and the density contrast ranged from 260-405 kg/m^3. The fault dip is similar to other cases as well, ranging between 24 and 35°. The histograms in this case showed

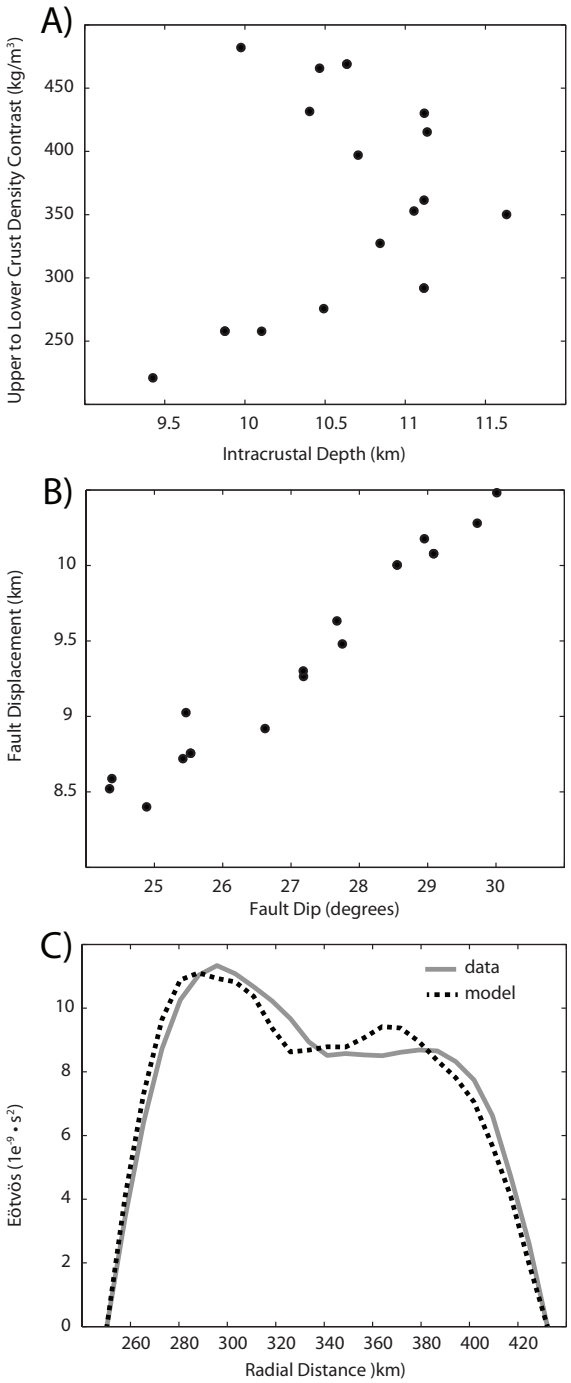

Figure 4.11: Model Results for Sector 1 shown in figure 1. RMS mifit ranges from 0.604 to 0.757 Eötvös. A) Density contrast across intracrustal interface vs. intracrustal interface depth. B) Vertical fault displacement vs. fault dip. C) Best- fit model from all models ran.

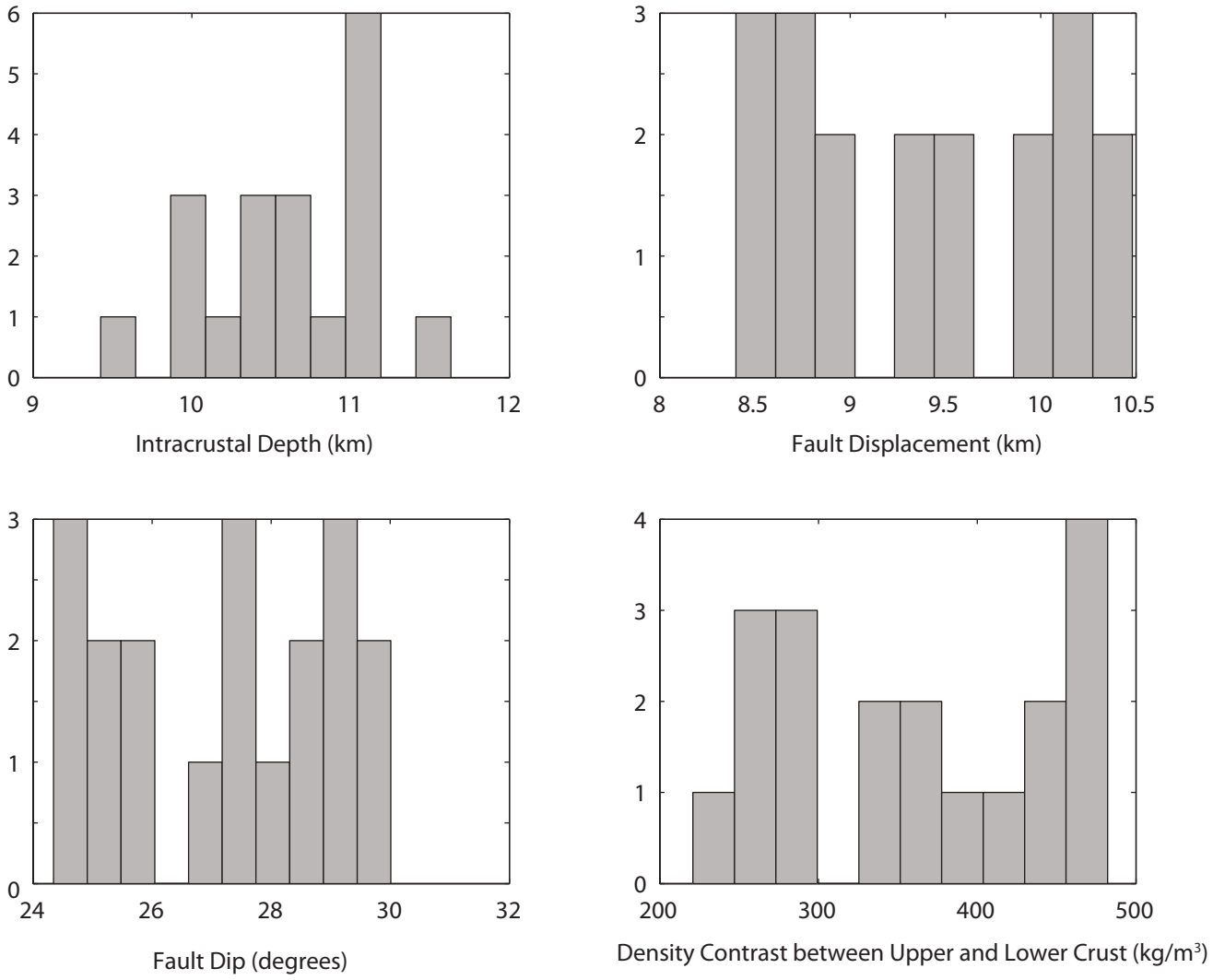

Figure 4.12: Histogram for the parameters of the best-fit solutions in the 20 models run in the case of using data from sector 1

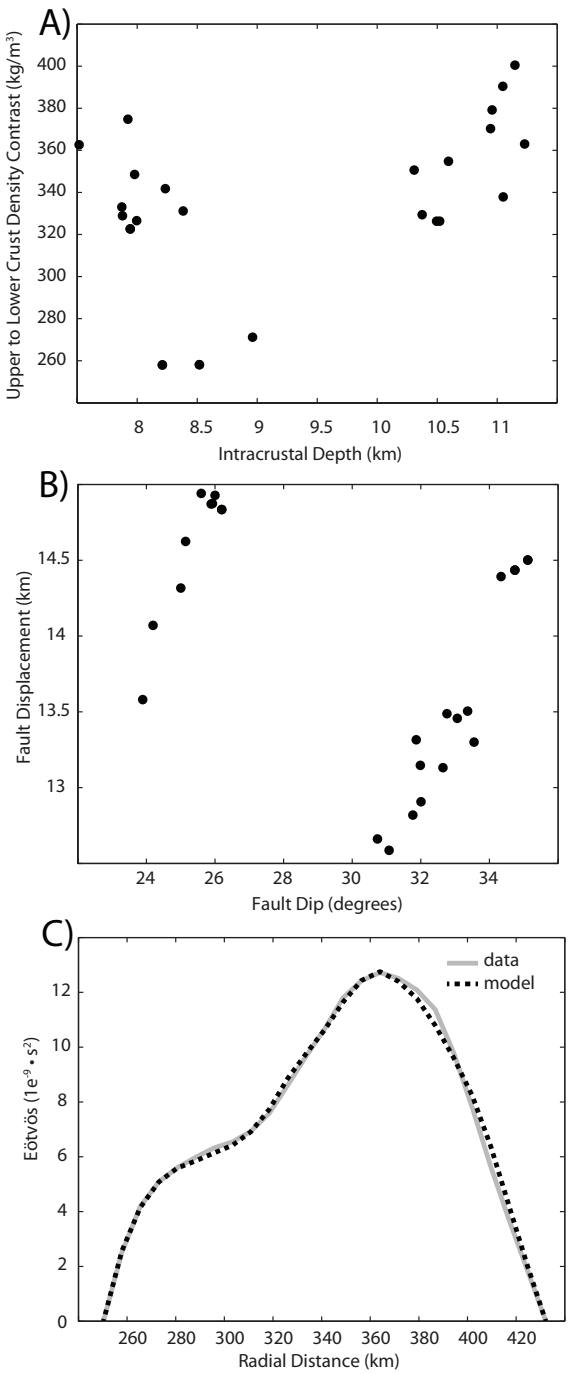

Figure 4.13: Model Results for Sector 2 shown in figure 1. RMS misfit ranges from 0.260 to 0.318 Eötvös. A) Density contrast across intracrustal interface vs. intracrustal interface depth. B) Vertical fault displacement vs. fault dip. C) Best- fit model from all models ran.

bimodal distributions (Figure 4.14) in all parameters from the 20 best-fit models. The misfit

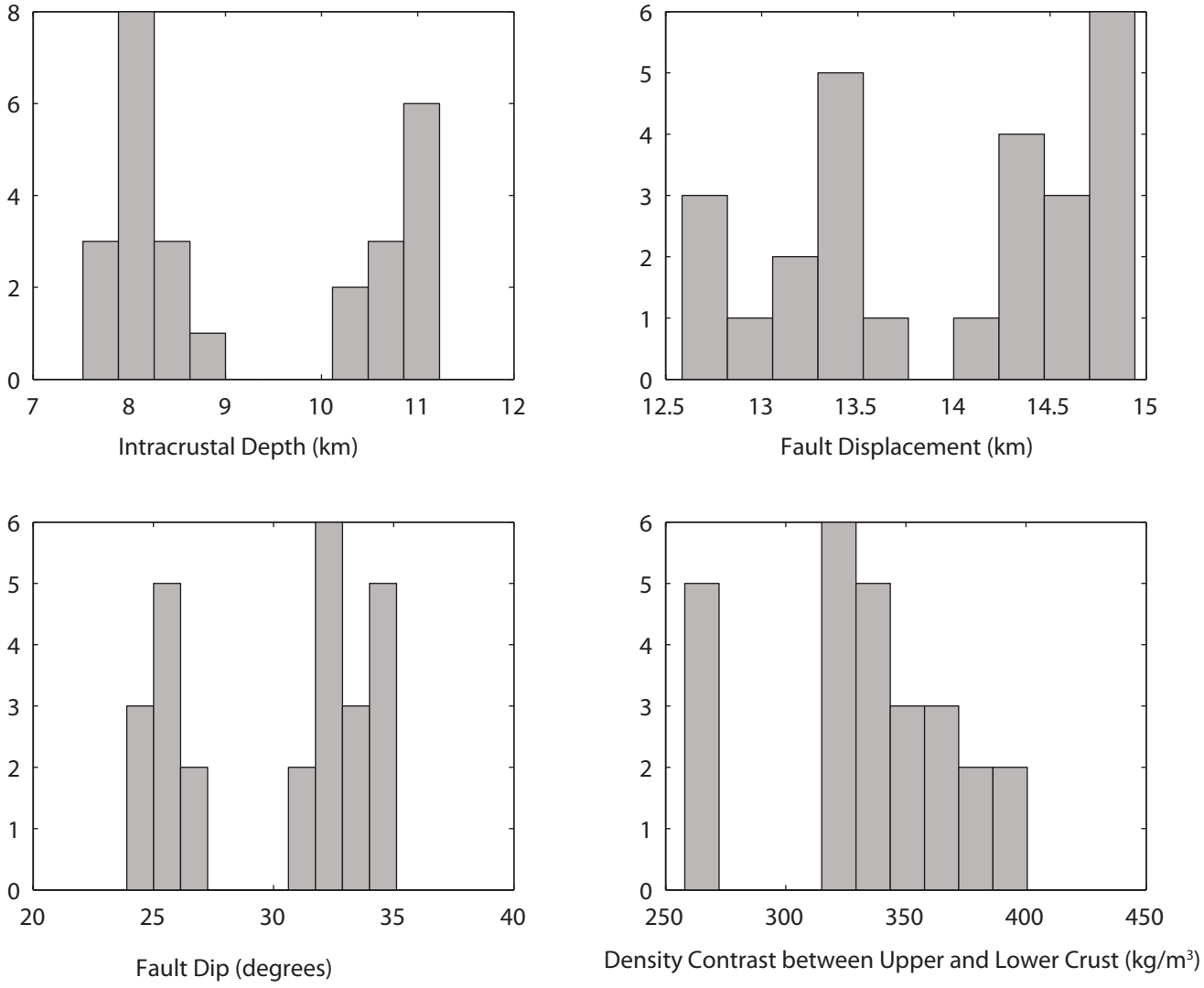

Figure 4.14: Histogram for the parameters of the best-fit solutions in the 20 models run in the case of using data from sector 2.

ranges obtained here were lower than those obtained within sector 1 and more comparable to the misfits in the other scenarios. The RMS misfits for all solutions ranges between 0.260 and 0.318 Eötvös. The two well separated clusters here indicate two local minima or one elongated and irregular global minimum. The best-fit solution ($\phi = 0.260$ Eötvös) obtained for sector 2 had an intracrustal interface depth of 7.8 km, a fault displacement of 14.8 km, a density contrast of 328 kg/m^3 between upper and lower crust, and a dip of 26° (Fig-

ure 4.13c). This best-fit model matched the data quite well, in contrast to the result from sector 1. The range of model solutions in this case that fell below the 1-σ error level within the data had intracrustal interface depth ranges of 7.5-20.6 km, fault displacements between 10.9-15 km, dips of 22.2-60.3 °, and densities of 173-426 $\mathrm{kg/m^3}$.

CHAPTER 5
DISCUSSION/CONCLUSION

This analysis has provided a quantitative test of the properties of ring faults extending into the subsurface of Orientale basin. The various scenarios tested span several subsurface structure possibilities, including faults at the Outer Rook and Cordillera, faults at the Cordillera only, and faults that do not cross the Moho. Despite the limitations of the current low-resolution gravity data, we have been able to place some constraints on the properties of the faults. We can confidently conclude that the inflections in the Bouguer gravity gradients are best explained by the presence of faults offsetting density interfaces in the subsurface. In all cases, solutions with shallow dip angles were preferred. Although the dip is similar in most cases, this result is mainly controlled by the intersection point of the faults with the surface and the depth of the intracrustal interface. Initializing the faults at different points in the surface will change the dip accordingly. Some uncertainty exists in where the faults actually initiate due to post-impact modification of the basin. Similarly, increasing the depth to the intracrustal interface would result in steeper dips. However, this decreases the magnitude of the resulting gravity anomalies at the surface, and all models clearly favor a shallow interface and low dip angle.

This analysis has shown that the observed gradient of the Bouguer anomaly is consistent with the effects of faults within the subsurface. The results are also supported by the fact that the best-fit fault displacements are reasonable matches to the topographic relief across the ring scarps, and the best-fit density contrasts are consistent with expectations based on plagioclase/anorthosite-rich upper crust and noritic lower crust. There is, however, some uncertainty as to whether both the Outer Rook and Cordillera faults exist, as the model excluding the Outer Rook fault provides a comparable fit to the data. As mentioned earlier, the detection of the Outer Rook fault within the subsurface is difficult due to the large

gravity anomaly in the center of the basin. Higher resolution gravity data from GRAIL (Zuber et al., 2012) may succeed in detecting the Outer Rook fault. However, models with no faults, including only the simple initial basin structure assumed, did not provide an acceptable fit to the data (Figure 4.10). Although we cannot exclude the possibility that smooth undulations in the relief along the Moho and intracrustal interface mimic the effects faults in the gravity, this scenario is unlikely and particularly unsatisfying given the clear fault scarps in the surface topography (Nahm & Kring, 2011).

Though not tested here, an interesting case would be to allow different displacements in the solution for both the Outer Rook fault and the Cordillera fault. This case is not considered here because the extra parameter would cause a slower convergence. However, the results with and without the Outer Rook fault show that the fit to the data is not strongly sensitive to the presence of this fault, and thus one would expect the results at the Cordillera to be only weakly dependent on the displacement at the Outer Rook fault. Another possibility is that the two faults may have different dips. Once again, the introduction of another parameter would cause a slower convergence.

The density contrast exerted a dominant control over the values that other parameters took on. In the four cases examined, a weak clustering of solutions into high and low density contrast groups was observed, with similar clustering of other parameters. The higher density contrast solutions also exhibited larger intracrustal interface depths and lower fault displacements. It is not immediately clear why high and low density contrast solutions provided better fits than the intermediate values. The lower density contrast clusters of 260-360 kg/m^3 provide a better match to previous work that suggested a density contrast of 400 kg/m^3 between the upper and lower crust (Wieczorek & Phillips, 1999). However, there is significant uncertainty in the densities of both the upper and lower crust.

The results in all cases support a shallow intracrustal interface. Though the predicted depths of 8-17 km are less than the 20 km depth found in the early analyses of the Apollo seismic experiments (Toksösz et al., 1974), the values agree well with the range of depths for

a density increase in the crust from more recent analyses (Lognonne et al., 2003). However, Orientale is far from the lunar seismic stations, and any lateral variability in the thickness of the upper crust would preclude a direct comparison. While this study assumed a single discrete density interface. A case that may be interesting to test in the future is the possibility of multiple density interfaces or a continuous gradational increase in density. Furthermore, the introduction of a three-layered crust (Bussey & Spudis, 2000) including a more mafic upper layer may affect the solution. However, the introduction of several interfaces within the subsurface introduces more free parameters in the model space and would significantly slow the convergence to a best-fit solution. The results of this study demonstrate that these more complicated scenarios are not required to match the data, but they cannot be excluded.

This analysis has been the first to quantitatively evaluate the evidence for ring faults in Orientale through gravity data. Other workers are undertaking a similar analysis, focusing on the topographic effects of ring tectonism (Nahm & Kring, 2011). Regarding the mechanism of basin ring formation, the close fit of the model predictions to the data argues strongly for the presence of a ring fault beneath the Cordillera, which is at odds with the frozen tsunami hypothesis. The inferred fault beneath the Cordillera is consistent with both the ring tectonics model of Melosh & McKinnon (1978) and the mega-terrace/nested melt cavity model of Head (1974, 2010).

Higher resolution and accurate gravity data from GRAIL will likely revise these results considerably, and more tightly constrain the subsurface geometry. The need for improved data is highlighted by the broad range of parameter space allowed at the 1-σ confidence level for the full azimuthal average. This study has developed a method that can be applied to the GRAIL data. GRAIL may also permit similar analyses on individual profiles without requiring averaging over large sectors of the basin. Future inversions of gravity data in other basins may further improve our understanding of multi-ring basin formation.

REFERENCES CITED

Andrews-Hanna, J. C. 2012. The Origin of Non-Mare Mascon Gravity Anomalies on the Moon. LPI Contributions, **43**, 2804.

Andrews-Hanna, J. C., & Stewart, S. T. 2011. The Crustal Structure of Orientale and Implications for Basin Formation. LPI Contributions, **42**, 2194.

Baldwin, R. B. 1981. On the tsunami theory of the origin of multi-ring basins. LPI Contributions, **12**, 275–288.

Baldwin, Ralph B. 1972. The tsunami model of the origin of ring structures concentric with large lunar craters. Physics of the Earth and Planetary Interiors, **6**(5), 327–339.

Baldwin, Ralph Belknap. 1949. The face of the moon. Univ. of Chicago Press.

Baldwin, Ralph Belknap. 1963. The measure of the moon. Univ. of Chicago Press.

Barbosa, Valeria C. F., Menezes, Paulo T. L., & Silva, Joo B. C. 2007. Gravity data as a tool for detecting faults: In-depth enhancement of subtle Almada's basement faults, Brazil. Geophysics, **72**(3), B59–B68.

Blakely, Richard J. 1996. Potential Theory in Gravity and Magnetic Applications. Cambridge University Press.

Bussey, D. Ben J., & Spudis, Paul D. 2000. Compositional studies of the Orientale, Humorum, Nectaris, and Crisium lunar basins. Journal of Geophysical Research, **105**(E2), 4235–4243.

Dorn, W. G. Van. 1968. Tsunamis on the Moon? Nature, **220**(5172), 1102–1107.

Dorn, W. G. Van. 1969. Lunar Maria: Structure and Evolution. Science, **165**, 693–695.

Fassett, Caleb I., Head, James W., Smith, David E., Zuber, Maria T., & Neumann, Gregory A. 2011. Thickness of proximal ejecta from the Orientale Basin from Lunar Orbiter Laser Altimeter (LOLA) data: Implications for multi-ring basin formation. Geophysical Research Letters, **38**, 17201.

Grieve, R. A. F., & Cintala, M. J. 1992. An analysis of differential impact melt-crater scaling and implications for the terrestrial impact record. Meteoritics, **27**, 526–538.

Hartmann, W. K., & Wood, C. A. 1971. Moon: Origin and evolution of multi-ring basins. The Moon, **3**(1), 3–78.

Hawke, B. R., Lucey, P. G., Taylor, G. J., Bell, J. F., Peterson, C. A., Blewett, D. T., Horton, K., Smith, G. A., & Spudis, P. D. 1991. Remote sensing studies of the Orientale Region of the Moon: A preGalileo view. Geophysical Research Letters, **18**(11), 2141–2144.

Hawke, B. R., Peterson, C. A., Blewett, D. T., Bussey, D. B. J., Lucey, P. G., Taylor, G. J., & Spudis, P. D. 2003. Distribution and modes of occurrence of lunar anorthosite. Journal of Geophysical Research, **108**(E6), 5050.

Head, J. W. 1974. Orientale multi-ringed basin interior and implications for the petrogenesis of lunar highland samples. Moon, **11**, 327–356.

Head, J. W. 2010. Transition from complex craters to multi-ringed basins on terrestrial planetary bodies: Scale-dependent role of the expanding melt cavity and progressive interaction with the displaced zone. Geophysical Research Letters, **37**, L02203.

Hikida, Hajime, & Wieczorek, Mark A. 2007. Crustal thickness of the Moon: New constraints from gravity inversions using polyhedral shape models. Icarus, **192**(1), 150–166.

Huang, Qian, & Wieczorek, Mark A. 2012. Density and porosity of the lunar crust from gravity and topography. Journal of Geophysical Research, **117**(E5), E05003.

Jolliff, Bradley L., Gillis, Jeffrey J., Haskin, Larry A., Korotev, Randy L., & Wieczorek, Mark A. 2000. Major lunar crustal terranes: Surface expressions and crust-mantle origins. Journal of Geophysical Research, **105**(E2), 4197–4216.

Khan, A., Mosegaard, K., & Rasmussen, K. L. 2000. A new seismic velocity model for the Moon from a Monte Carlo inversion of the Apollo lunar seismic data. Geophysical Research Letters, **27**(11), 1591–1594.

Kiefer, Walter S., Macke, Robert J., Britt, Daniel T., Irving, Anthony J., & Consolmagno, Guy J. 2012. The density and porosity of lunar rocks. Geophysical Research Letters, **39**(7), L07201.

Klingel, E. E., Marson, I., & Kahle, H.-G. 1991. Automatic Interpretation of Gravity Gradiometric Data in Two Dimensions: Vertical Gradient. Geophysical Prospecting, **39**(3), 407–434.

Lognonne, Philippe, Gagnepain-Beyneix, Jeannine, & Chenet, Hugues. 2003. A new seismic model of the Moon: implications for structure, thermal evolution and formation of the Moon. Earth and Planetary Science Letters, **211**(1), 27–44.

Mazarico, E., Lemoine, F. G., Han, Shin-Chan, & Smith, D. E. 2010. GLGM-3: A degree-150 lunar gravity model from the historical tracking data of NASA Moon orbiters. Journal of Geophysical Research, **115**, 14.

Melosh, H. J. 1989. Impact cratering: A geologic process. Oxford Univ. Press.

Melosh, H. J., & McKinnon, William B. 1978. The mechanics of ringed basin formation. Geophysical Research Letters, **5**(11), PP. 985–988.

Mosegaard, Klaus, & Tarantola, Albert. 1995. Monte Carlo sampling of solutions to inverse problems. Journal of Geophysical Research, **100**(B7), 12431–12447.

Nahm, A. L., & Kring, D. A. 2011. Evidence of Normal Faulting of the Outer Rings of Orientale Basin: Preliminary Modeling Results. LPI Contributions, **42**, 1172.

Nakamura, Y. 1983. Seismic velocity structure of the lunar mantle. Journal of Geophysical Research, **88**, 677–686.

Neumann, Gregory A., Zuber, Maria T., Smith, David E., & Lemoine, Frank G. 1996. The lunar crust: Global structure and signature of major basins. Journal of Geophysical Research, **101**(E7), 16841–16843.

Osinski, Gordon R., & Spray, John G. 2005. Tectonics of complex crater formation as revealed by the Haughton impact structure, Devon Island, Canadian High Arctic. Meteoritics & Planetary Science, **40**(12), 1813–1834.

Pieters, C. M., Iii, J. W. Head, Gaddis, L., Jolliff, B., & Duke, M. 2001. Rock types of South Pole-Aitken basin and extent of basaltic volcanism. Journal of Geophysical Research, **106**(E11), 28001–28022.

Sambridge, Malcolm, & Mosegaard, Klaus. 2002. Monte Carlo methods in geophysical inverse problems. Reviews of Geophysics, **40**(3), 1009.

Scholz, C H. 2002. The Mechanics of Earthquakes and Faulting, 2nd ed. Cambridge Univ. Press.

Schultz, P. H., Miller, B., Orphal, D., Borden, W. F., & Larson, S. A. 1981. Multi-ring basin formation - Possible clues from impact cratering calculations. LPI Contributions, 181–195.

Shearer, C. K., & Papike, J. J. 1999. Magmatic evolution of the Moon. American Mineralogist, **84**(10), 1469–1494.

Shi, Jian-Chun, Ma, Yue-Hua, & Bao, Gang. 2009. The Formation Model of Multi-ring Basins Based on the Theory of Impact Tsunami. Chinese Astronomy and Astrophysics, **33**(3), 287–292.

Smith, David E., Zuber, Maria T., Neumann, Gregory A., Lemoine, Frank G., Mazarico, Erwan, Torrence, Mark H., McGarry, Jan F., Rowlands, David D., Iii, James W. Head, Duxbury, Thomas H., Aharonson, Oded, Lucey, Paul G., Robinson, Mark S., Barnouin, Olivier S., Cavanaugh, John F., Sun, Xiaoli, Liiva, Peter, Mao, Dan-dan, Smith, James C., & Bartels, Arlin E. 2010. Initial observations from the Lunar Orbiter Laser Altimeter (LOLA). Geophysical Research Letters, **37**(18), L18204.

Smith, J. V., Anderson, A. T., Newton, R. C., Olsen, E. J., Crewe, A. V., Isaacson, M. S., Johnson, D., & Wyllie, P. J. 1970. Petrologic history of the moon inferred from petrography, mineralogy and petrogenesis of Apollo 11 rocks. Geochimica et Cosmochimica Acta Supplement, **1**, 897.

Spudis, Paul D. 2005. The Geology of Multi-Ring Impact Basins. Cambridge University Press.

Spudis, Paul D., Hawke, B. Ray, & Lucey, Paul. 1984. Composition of Orientale Basin Deposits and Implications for the Lunar Basin-Forming Process. Journal of Geophysical Research, **89**(S1), C197–C210.

Toksösz, M. Nafi, Dainty, Anton M., Solomon, Sean C., & Anderson, Kenneth R. 1974. Structure of the Moon. Reviews of Geophysics, **12**(4), 539–567.

Warren, Paul H., & Wasson, John T. 1979. The origin of KREEP. Reviews of Geophysics, **17**(1), 73–88.

Wieczorek, Mark A., & Phillips, Roger J. 1997. The structure and compensation of the lunar highland crust. Journal of Geophysical Research, **102**(E5), 10933–10943.

Wieczorek, Mark A., & Phillips, Roger J. 1998. Potential anomalies on a sphere - Applications to the thickness of the lunar crust. Journal of Geophysical Research, **103**, 1715.

Wieczorek, Mark A., & Phillips, Roger J. 1999. Lunar Multiring Basins and the Cratering Process. Icarus, **139**, 246–259.

Wieczorek, Mark A., & Phillips, Roger J. 2000. The "Procellarum KREEP Terrane": Implications for mare volcanism and lunar evolution. Journal of Geophysical Research, **105**(E8), 20417–20430.

Wieczorek, Mark A., Jolliff, Bradley L., Khan, Amir, Pritchard, Matthew E., Weiss, Benjamin P., Williams, James G., Hood, Lon L., Righter, Kevin, Neal, Clive R., Shearer, Charles K., McCallum, I. Stewart, Tompkins, Stephanie, Hawke, B. Ray, Peterson, Chris, Gillis, Jeffrey J., & Bussey, Ben. 2006. The Constitution and Structure of the Lunar Interior. Reviews in Mineralogy and Geochemistry, **60**(1), 221–364.

Williams, Kevin K., & Zuber, Maria T. 1998. Measurement and Analysis of Lunar Basin Depths from Clementine Altimetry. Icarus, **131**(1), 107–122.

Wood, J. A., Dickey, J. S., Marvin, Ursula B., & Powell, B. N. 1970. Lunar anorthosites and a geophysical model of the moon. Geochimica et Cosmochimica Acta Supplement, **1**, 965.

Woodruff, W. F., Revil, A., Jardani, A., Nummedal, D., & Cumella, S. 2010. Stochastic Bayesian inversion of borehole self-potential measurements. Geophysical Journal International, **183**(2), 748–764.

Yue, Zeng-Yuan, Zhang, Bin, & Chen, Dao-Han. 1990. On the tsunami model of the origin of multi-ring basins. Earth Moon and Planets, **49**, 253–258.

Zuber, M. T., Smith, D. E., Asmar, S. W., Konopliv, A. S., Lemoine, F. G., Melosh, H. J., Neumann, G. A., Phillips, R. J., Solomon, S. C., Watkins, M. M., Wieczorek, M. A., Williams, J. G., Head, J. W., Mazarico, E., & Torrence, M. H. 2012. Preliminary Results on the Structure of Lunar Highland Crust from GRAIL Gravity and LOLA Altimetry. LPI Contributions, **1677**, 69–70.